

Asymptotic analysis of the Boltzmann–BGK equation for oscillatory flows

Jason Nassios¹ and John E. Sader^{1,2,†}

¹ Department of Mathematics and Statistics, The University of Melbourne, Victoria 3010, Australia

² Kavli Nanoscience Institute and Department of Physics, California Institute of Technology, Pasadena, CA 91125, USA

(Received 12 January 2012; revised 2 May 2012; accepted 13 June 2012;
first published online 10 August 2012)

Kinetic theory provides a rigorous foundation for calculating the dynamics of gas flow at arbitrary degrees of rarefaction, with solutions of the Boltzmann equation requiring numerical methods in many cases of practical interest. Importantly, the near-continuum regime can be examined analytically using asymptotic techniques. These asymptotic analyses often assume steady flow, for which analytical slip models have been derived. Recently, developments in nanoscale fabrication have stimulated research into the study of oscillatory non-equilibrium flows, drawing into question the applicability of the steady flow assumption. In this article, we present a formal asymptotic analysis of the unsteady linearized Boltzmann–BGK equation, generalizing existing theory to the oscillatory (time-varying) case. We consider the near-continuum limit where the mean free path and oscillation frequency are small. The complete set of hydrodynamic equations and associated boundary conditions are derived for arbitrary Stokes number and to second order in the Knudsen number. The first-order steady boundary conditions for the velocity and temperature are found to be unaffected by oscillatory flow. In contrast, the second-order boundary conditions are modified relative to the steady case, except for the velocity component tangential to the solid wall. Application of this general asymptotic theory is explored for the oscillatory thermal creep problem, for which unsteady effects manifest themselves at leading order.

Key words: kinetic theory, MEMS/NEMS, non-continuum effects

1. Introduction

The Navier–Stokes equations together with the no-slip boundary condition provide a rigorous framework for studying many flow phenomena, including turbulence (Reynolds 1895; Batchelor 1953; Ashurst *et al.* 1987; Clercx & van Heijst 2009), oscillatory flows (Stokes 1851; Pozrikidis 1992), boundary layer effects (Prandtl 1904; Schlichting 1960), and pipe and channel flows (Reynolds 1883; Orszag & Kells 1980). Applicability of the Navier–Stokes equations and no-slip condition is contingent on validity of the continuum approximation. Miniaturization or operation at low gas densities can lead to violation of this fundamental tenet. The degree of gas rarefaction can be captured by the Knudsen number, Kn , defined as the ratio of the mean free

† Email address for correspondence: jsader@unimelb.edu.au

path λ to the characteristic length scale of the flow L_c :

$$Kn = \frac{\lambda}{L_c}. \quad (1.1)$$

Maxwell (1878) showed that rarefaction effects in a gas could be modelled by allowing for velocity slip at the boundaries (assumed to be solid walls), and presented the first of many slip models for rarefied flows (Weng & Chen 2008). This area has received significant attention of late, motivated by the need to model flow phenomena in micro- and nanoscale devices, e.g. those encountered in nanoelectromechanical systems (NEMS). These modern devices have many applications, including ultra-fine scale mass measurement (Craighead 2000; Cleland 2002; Yang *et al.* 2006; Bargatin, Kozinsky & Roukes 2007; Burg *et al.* 2007), fluid property detection (Sader 1998; Boskovic *et al.* 2002; Motamedi & Wood-Adams 2010), sensing of environmental conditions (Berger *et al.* 1997; Lavrik, Sepaniak & Datskos 2004), and atomic resolution imaging (Binnig, Quate & Gerber 1986; Giessibl 2003). The flows generated by these small devices are often oscillatory and some lie outside the realm of standard continuum theory. For example, these devices can exhibit oscillation frequencies in the microwave range and length scales comparable to the gas mean free path, rendering invalid the fundamental assumptions of this classical theory.

Solutions to non-equilibrium gas flows have been widely reported, and are primarily based on an analysis of the Boltzmann equation (Boltzmann 1872) or an associated model equation, the Boltzmann–BGK equation (Bhatnagar, Gross & Krook 1954; Welander 1954). The derivation of these equations utilizes particle conservation principles, ensuring their general applicability over all oscillation frequencies and length scales. Direct analysis of the Boltzmann equation is complicated by the nature of the collision integral (Cercignani 2000). The BGK approximation retains the qualitative properties of the collision operator and simplifies the analysis of many significant gas flows (Cercignani 2000). The validity of the approximation is contingent on the assumption of a uniform collision frequency, which is valid provided temperature perturbations in the gas are small. A well-documented shortcoming of the Boltzmann–BGK equation is that the correct Prandtl number for monatomic gases is not recovered (Cercignani 1988; Sone 2000). Despite these issues, the BGK approximation is widely applied and has proved to be an important tool in many theoretical investigations (see Cercignani 2000 and Sone 2000). As such, this article focuses on the Boltzmann–BGK equation.

Asymptotic analyses of both the Boltzmann and Boltzmann–BGK equations have been undertaken to probe the near-continuum regime. Pioneering methods include the Hilbert and Chapman–Enskog expansions (Hilbert 1900, 1912; Chapman 1916; Enskog 1917). We explore a generalization of the former procedure in this article. Grad’s moment method can also be used to generate hydrodynamic equations that characterize non-equilibrium flows (Grad 1949, 1958). Numerical schemes in use today primarily implement Monte Carlo methods, in particular the direct simulation Monte Carlo (DSMC) method (Bird 1963). More recently, the lattice Boltzmann (LB) method has been investigated (McNamara & Zanetti 1988; Higuera & Jiménez 1989).

The DSMC method was originally developed by Anderson and Lord Kelvin (Bird 1978). The method simulates gas flows using the collisional dynamics of the constituent particles (Bird 1998). In this regard, DSMC has found widespread application in analysing flows for a variety of intermolecular potentials. However, at the low Mach numbers intrinsic to nanoscale systems, statistical noise can dominate these numerical solutions (Hadjiconstantinou *et al.* 2003). Techniques have

also been proposed to minimize noise at low Mach numbers (Fan & Shen 2001; Baker & Hadjiconstantinou 2005; Chun & Koch 2005; Baker & Hadjiconstantinou 2008; Ramanathan & Koch 2009; Ramanathan, Koch & Bhiladvala 2010; Radtke, Hadjiconstantinou & Wagner 2011).

The origins of the LB method are more recent, evolving from the lattice gas cellular automata (LGCA) model (Frisch, Hasslacher & Pomeau 1986). The first formal LB algorithm appeared just over two decades ago, and was later simplified through the use of the Boltzmann–BGK equation (McNamara & Zanetti 1988; Higuera & Jiménez 1989; Chen *et al.* 1991; Qian, D’Humières & Lallemand 1992). The LB method is now used to study a diverse range of flow problems (Chen *et al.* 2003; Yu, Girimaji & Luo 2005; Shi & Sader 2010). Most recently, its applicability to rarefied gas flows has also been explored (Colosqui *et al.* 2010; Shi *et al.* 2011; de Izarra, Rouet & Izrar 2011).

The Chapman–Enskog method provides a link between kinetic theory and gas hydrodynamics (Chapman 1916; Enskog 1917; Chapman & Cowling 1960; Cercignani 2000; Sone 2000). In this method, a formal asymptotic expansion of the Boltzmann equation is sought for rarefied flows in the continuum limit, via an expansion of the distribution function and the streaming operator. The result is a series of hydrodynamic equations at successive orders of Knudsen number. One recovers the Euler equations to leading order and the Navier–Stokes equations of continuum flow to first order. At subsequent orders, the hydrodynamic equations are the Burnett and super-Burnett equations (Burnett 1935; Chapman & Cowling 1960; Shavaliyev 1993; Agarwal, Yun & Balakrishnan 2001).

Issues regarding these higher-order Burnett equations remain. The instability of the Burnett and super-Burnett equations has been the focus of considerable research (Bobylev 1982; Struchtrup & Torrilhon 2003; Struchtrup 2005). While methods have been discussed to regularize or stabilize these equations (Zhong, MacCormack & Chapman 1993; Jin & Slemrod 2001; Soderholm 2007), their applicability in a general context has not been established. Second, these higher-order differential equations require additional boundary conditions to determine their unique solution (Lee 1994; Agarwal *et al.* 2001). Numerous methods and models have been proposed to resolve this issue (Maurer *et al.* 2003; Shen *et al.* 2007; Gu & Emerson 2007; Torrilhon & Struchtrup 2008). While the Chapman–Enskog procedure provides us with a means to derive higher-order bulk flow equations, there remains no consensus on a systemic approach to solve the associated boundary value problem.

Grad’s moment method (Grad 1949, 1958) bypasses the solution for the mass distribution function by taking moments of the Boltzmann or Boltzmann–BGK equation (Torrilhon & Struchtrup 2008). However, the resulting set of moment equations are coupled, and appropriate closures and boundary conditions must be derived. These issues have been addressed by Struchtrup & Torrilhon (2003), Torrilhon & Struchtrup (2008) and Groth & McDonald (2009).

Hilbert proposed a method for solving the Boltzmann equation using a formal asymptotic expansion in the Knudsen number (Hilbert 1900, 1912). To leading order in the Knudsen number, the method recovers the Euler equations for inviscid flow as the governing hydrodynamic equations. At higher order, the Euler equations reappear, but now with forcing terms related to lower-order stresses and heat flows (Sone 2000). Interestingly, the classical (nonlinear) Navier–Stokes equations never arise (Sone 2000). The relevant boundary conditions to apply at each order in the Knudsen number remained unresolved at the time of Hilbert (Hilbert 1900, 1912; Cercignani 2000; Sone 2000).

Cercignani addressed this issue and derived tangential velocity boundary conditions directly from the linearized Boltzmann–BGK equation for the first- and second-order (steady) hydrodynamic equations (Cercignani 1962, 1964). Sone elaborated on this approach and derived a general set of boundary conditions for linearized steady flow over simple (i.e. rigid) solid walls (Sone 1969, 1974). Incident particles were assumed to undergo diffuse reflection from these walls with zero net mass flux. The shape or curvature of the walls was considered arbitrary, the only restriction being that they were smooth. The bulk flow equations (away from any surface) were derived using the classical Hilbert expansion, which recovered the Stokes equations for creeping flow at each order in the Knudsen number – non-equilibrium effects did not alter the macroscopic hydrodynamic equations. To account for the Knudsen layer near the surface, a matched asymptotic expansion was performed for small Knudsen number, with the surface geometry characterized by the method of moving frame (Cartan 1977; Sone 2000). The anisotropy of space within the boundary layer resulted in an infinite set of integral equations, which were solved simultaneously using numerical methods up to second order in the Knudsen number (Sone 1964, 1965; Sone & Onishi 1973). This asymptotic formulation recovered the no-slip condition as the unique boundary condition in the continuum limit, and the slip models derived by Cercignani at first and second order (Sone 1968*b*, 1969). Furthermore, the set of higher-order slip conditions contained thermal gradient terms whose presence was later verified experimentally (see Sone 2000). Corrective terms to account for curvature effects of the solid walls also appeared, and were subsequently confirmed for microscale flows (Tibbs, Baras & Garcia 1997). This resolved the boundary value problem originally encountered by Hilbert (Hilbert 1900, 1912; Cercignani 2000). The theory assumed steady flow at low Mach and Reynolds number.

While many of the assumptions underlying Sone’s original theory have since been relaxed, e.g. the low Mach and Reynolds number restrictions, the effect of unsteadiness is yet to be fully explored (Sone & Onishi 1978; Onishi & Sone 1979; Ohwada, Sone & Aoki 1989*a,b*; Sone, Ohwada & Aoki 1989; Ohwada & Sone 1992). Some canonical unsteady flows have been considered, such as Stokes’ second problem and the linearized Rayleigh problem (Sone 1964, 1965, 1968*a*). The influence of time-dependence on the bulk flow has also been investigated for the hard-sphere Boltzmann equation (Bardos, Golse & Levermore 1993, 1998; Sone 2007). Interestingly, unsteady effects have been shown to not affect the existing steady boundary conditions and Knudsen layer corrections to first order in the Knudsen number (Sone 2007). The effect of unsteadiness on the full hydrodynamic equation/boundary condition set, up to and including second order in the Knudsen number, is yet to be investigated. Second-order models have received considerable attention recently, particularly in the context of oscillatory flows (Hadjiconstantinou 2003, 2005*b*; Cao *et al.* 2009; Pitakarnnop *et al.* 2009). Interestingly, Hadjiconstantinou’s numerical studies have suggested that unsteady motion does not affect the second-order tangential slip model (Hadjiconstantinou 2005*b*). A mathematical proof of this suggestion is yet to appear. More recently, Takata *et al.* (2012) presented a formal asymptotic analysis of the unsteady (linear in time, t) heating of two parallel plane walls. They show that unsteady heating of this form results in a modification of the classical second-order steady temperature slip model derived by Sone (1974).

In this article, we present a formal asymptotic analysis of the Boltzmann–BGK equation for oscillatory flows in a slightly rarefied gas, i.e. small Knudsen numbers. In so doing, we elucidate the effect of unsteadiness on the bulk flow hydrodynamic equations and their associated boundary conditions. This is performed up to and

including equations second-order in the Knudsen number. Our analysis is restricted to low Mach and Reynolds number flow; all perturbations in the macroscopic quantities about their equilibrium values are thus small. This permits linearization of the governing equation and boundary conditions, and justifies the assumption of uniform gas collision frequency implicit in the BGK approximation. Numerical techniques have been proposed and applied to analyse solutions of the linearized Boltzmann–BGK equation for some canonical oscillatory rarefied gas flows (Sharipov & Kalempa 2007, 2008; Manela & Hadjiconstantinou 2010; Yap & Sader 2012). While these analyses provide high-accuracy data sets for linearized problems of immense practical importance, analytical expressions provide additional insight into the underlying physics driving the gas flows. The work we present in this article provides the essential generalization to the original steady asymptotic theory of Sone (1969, 1974).

We prove that oscillatory motion leads to compressible bulk flow at first order in the Knudsen number; non-isothermal flows are also shown to evolve according to a modified Navier–Stokes equation. In contrast, both isothermal and non-isothermal flows obey a (different) modified Navier–Stokes equation at second order in the Knudsen number. This feature is distinct from the well-known steady flow asymptotic theory (Cercignani 1962, 1964; Sone 1969, 1974), where the bulk flow equations are identical to the Stokes equations at all orders in the Knudsen number.

Tangential velocity slip models, up to and including second order in the Knudsen number, are found to be identical to those for steady flow. This validates the observation of Hadjiconstantinou (2005*b*), who suggested that the conventional (steady) second-order tangential slip model can be used to analyse oscillatory flows. Even so, other second-order components of the boundary conditions are modified by unsteady effects. In particular, we show that oscillatory (time-varying) heating results in a modification to the second-order temperature slip model that is equivalent to that presented in Takata *et al.* (2012). Our analysis is supplemented by additional terms, which account for non-zero boundary curvature, wall-normal velocity and gas compressibility effects, as we shall discuss. The leading-order effects of unsteadiness on gas rarefaction thus manifest themselves through the bulk flow equations, rather than their associated boundary conditions.

To demonstrate application of this theory, we study flows generated by oscillatory temperature gradients applied to two adjacent solid walls, i.e. thermal creep and transpiration. This generalizes the original work of Sone (1966), who considered the classical thermal creep problem of steady flow in an infinite half-space, due to a time-independent temperature gradient imposed along the wall (Reynolds 1879; Maxwell 1879; Kennard 1938).

This phenomenon has found applications in a wide range of contexts. For example, thermal transpiration in a circular pipe was considered by Sone (1968*b*) and Ohwada *et al.* (1989*b*), and subsequently applied to study of the Knudsen compressor (Knudsen 1909*a,b*; Loyalka 1971; Loyalka, Petrellis & Storvick 1979; Vargo *et al.* 1999). More recently, thermal creep has been proposed as a mechanism for motion of (volatile) Leidenfrost drops along a ratchet surface (Lagubeau *et al.* 2011; Würger 2011). In addition to its practical significance, the leading-order flow generated in the thermal creep problem occurs at $O(Kn)$. As discussed, the leading-order effect of unsteadiness in a rarefied flow also appears at $O(Kn)$ for non-isothermal flows. Consequently, we present a detailed analysis of the oscillatory (time-varying) thermal creep problem.

While several canonical shear-driven gas flows, e.g. oscillatory Couette flow, have been examined using a variety of numerical and analytical methods, these flows are isothermal in the linear limit (Park, Bahukudumbi & Beskok 2004; Hadjiconstantinou 2005a; Sharipov & Kalempa 2007, 2008; Tang *et al.* 2008). The leading-order effect of unsteadiness in these flows occurs via a modification to the classical Navier–Stokes description at second order in the Knudsen number, i.e. $O(Kn^2)$: this does not alter the leading-order shear flow. For this reason, we restrict ourselves to a detailed exposition of the thermal creep problem in this article.

Section 2 begins with a brief outline of the linearized Boltzmann–BGK equation and its derivation. Details of the matched asymptotic expansion, relevant curvature equations, and a discussion of the scaling analysis are then given. In § 3, we present a detailed exposition of the required asymptotic results for the bulk flow equations and boundary conditions up to second order in the Knudsen number. Key findings and formulas from the bulk flow analysis are summarized in § 3.1. The complete set of hydrodynamic equations, up to second order in the Knudsen number, are given in table 1. A discussion of the Knudsen layer analysis, up to first order in the Knudsen number, is presented in § 3.2.1, with the complete of associated Knudsen layer corrections and slip boundary conditions in table 2. Corresponding discussion and summary of the formulas at second order in the Knudsen number are given in § 3.2.2 and table 3, respectively. The Knudsen layer integral equations, Knudsen layer corrections, and slip coefficients are relegated to the Appendices. We conclude in § 4 by exploring the application of this theory to oscillatory thermal creep between two adjacent walls.

2. Theoretical framework

The mass distribution function of the gas, $F(\mathbf{x}, \mathbf{v}, t)$, is assumed to obey the Boltzmann–BGK equation (Bhatnagar *et al.* 1954; Welander 1954; Vincenti & Kruger 1965),

$$\frac{\partial F}{\partial t} + v_i \frac{\partial F}{\partial x_i} + a_i \frac{\partial F}{\partial v_i} = \nu (\rho(\mathbf{x}, t) f_0(\mathbf{v}) - F), \quad (2.1)$$

where the equilibrium velocity distribution function at the local temperature, $T(\mathbf{x}, t)$, and mean velocity, $\bar{\mathbf{v}}(\mathbf{x}, t)$, is

$$f_0(\mathbf{v}) = \left(\frac{1}{\sqrt{\pi} v_{mp}(T)} \right)^3 \exp \left(- \left[\frac{v_i - \bar{v}_i}{v_{mp}(T)} \right]^2 \right), \quad (2.2)$$

and t is time, ν is the particle collision frequency, k_B is Boltzmann’s constant, and \mathbf{x} , \mathbf{v} and \mathbf{a} are the particle position, particle velocity and body force, respectively. The most probable collision speed of gas molecules of mass m at temperature $T(\mathbf{x}, t)$ is defined as

$$v_{mp}(T) = \sqrt{\frac{2k_B T}{m}}, \quad (2.3)$$

and the local density is $\rho(\mathbf{x}, t)$. The local density ρ , mean gas velocity $\bar{\mathbf{v}}$ and temperature T are given by the following moments of the mass distribution

function,

$$\rho = \int_{-\infty}^{\infty} F \, d\mathbf{v}, \tag{2.4a}$$

$$\bar{\mathbf{v}} = \frac{1}{\rho} \int_{-\infty}^{\infty} \mathbf{v} F \, d\mathbf{v}, \tag{2.4b}$$

$$\frac{3k_B T}{m} = \frac{1}{\rho} \int_{-\infty}^{\infty} (\mathbf{v} - \bar{\mathbf{v}})^2 F \, d\mathbf{v}, \tag{2.4c}$$

$$\frac{p}{\rho} = \frac{k_B T}{m}, \tag{2.4d}$$

where the equation of state is the ideal gas law, and $p(\mathbf{x}, t)$ is the local pressure.

Mass, momentum and energy are conserved quantities over intermolecular collisions (Vincenti & Kruger 1965):

$$\begin{bmatrix} 0 \\ 0 \\ 0 \end{bmatrix} = \int_{-\infty}^{\infty} \begin{bmatrix} m \\ m\mathbf{v} \\ \frac{1}{2}m\mathbf{v}^2 \end{bmatrix} (\mathbf{v}[\rho(\mathbf{x}, t)f_0(\mathbf{v}) - F]) \, d\mathbf{v}. \tag{2.5}$$

We restrict our analysis to low Mach and Reynolds number flows. This permits linearization of the governing equation for F , its moments, and the collisional invariant relations about their respective equilibrium solutions. To proceed, we thus define

$$\rho = \rho_0 (1 + \sigma(\mathbf{x}, t)), \tag{2.6a}$$

$$T = T_0 (1 + \tau(\mathbf{x}, t)), \tag{2.6b}$$

$$p = p_0 (1 + P(\mathbf{x}, t)), \tag{2.6c}$$

$$F = \rho_0 E_0 (1 + \phi(\mathbf{x}, \mathbf{v}, t)), \tag{2.6d}$$

where ρ_0 , T_0 , p_0 and $\rho_0 E_0$ are the equilibrium density, temperature, pressure and mass distribution, respectively; the functions σ , τ , P and ϕ are perturbations to these equilibrium values. The function E_0 in (2.6) is given by

$$E_0 = \left(\frac{1}{\sqrt{\pi} v_{mp}(T_0)} \right)^3 \exp \left(- \left[\frac{v_i}{v_{mp}(T_0)} \right]^2 \right). \tag{2.7}$$

We then substitute (2.6) into (2.1), (2.4) and (2.5) and linearize the resulting system. This allows all time-varying functions to be expressed in terms of the explicit time-dependence,

$$\alpha(\mathbf{x}, \mathbf{v}, t) = \tilde{\alpha}(\mathbf{x}, \mathbf{v}) \exp(-i\omega t), \tag{2.8}$$

where i is the usual imaginary unit, ω is the radial frequency of oscillation, and α represents any of: (i) the perturbations in (2.6); (ii) the mean gas velocities \bar{v}_i ; or (iii) the body force a_i . The body force is thus regarded in general as oscillatory (time-varying). For simplicity we omit the ‘ \sim ’ notation used in (2.8); henceforth, all dependent functions are thus frequency-dependent expressions. This immediately leads to the required linearized Boltzmann–BGK equation for oscillatory flow,

$$-i\omega\phi + v_i \frac{\partial \phi}{\partial x_i} - \frac{2}{v_{mp}^2(T_0)} v_i a_i = v \left(\sigma - \phi + \frac{2}{v_{mp}^2(T_0)} \bar{v}_i v_i + \left[\left(\frac{v_i}{v_{mp}(T_0)} \right)^2 - \frac{3}{2} \right] \tau \right), \tag{2.9}$$

where the moment equations are

$$\sigma = \int_{-\infty}^{\infty} \phi E_0 \, d\mathbf{v}, \quad (2.10a)$$

$$\bar{v}_i = \int_{-\infty}^{\infty} v_i \phi E_0 \, d\mathbf{v}, \quad (2.10b)$$

$$\frac{3}{2}\tau = \int_{-\infty}^{\infty} \left(\left(\frac{v_i}{v_{mp}(T_0)} \right)^2 - \frac{3}{2} \right) \phi E_0 \, d\mathbf{v}, \quad (2.10c)$$

$$P = \sigma + \tau, \quad (2.10d)$$

with the collisional invariant relations in (2.4) taking the form

$$\begin{bmatrix} 0 \\ 0 \\ 0 \end{bmatrix} = \int_{-\infty}^{\infty} \begin{bmatrix} 1 \\ \mathbf{v} \\ \mathbf{v}^2 \end{bmatrix} \left(\sigma - \phi + \frac{2}{v_{mp}^2(T_0)} \bar{v}_i v_i + \left[\left(\frac{v_i}{v_{mp}(T_0)} \right)^2 - \frac{3}{2} \right] \tau \right) E_0 \, d\mathbf{v}. \quad (2.11)$$

2.1. Scaling and generalized coordinates

The following scales are chosen for the particle velocity v_i , mean velocity \bar{v}_i and bulk acceleration a_i ,

$$v_s = v_{mp}(T_0), \quad \bar{v}_s = v_{mp}(T_0), \quad a_s = v_{mp}(T_0)\omega, \quad (2.12)$$

where the subscript s denotes a scale. The scaling for a_i is appropriate for an oscillatory body force. Two length scales exist: the mean free path of the gas λ , and the geometric length scale of the solid L_c , which is assumed to be much larger than the mean free path. This separation of length scales results in a local flow near the solid surface, i.e. within the Knudsen layer, and a bulk flow away from the surface. The flows in these complementary regions will be solved for using a matched asymptotic expansion in the Knudsen number, $Kn \ll 1$.

The bulk flow is analysed via a classical Hilbert expansion, with isotropic length scale L_c (Hilbert 1900, 1912; Sone 1969, 1974; Cercignani 2000). Within the Knudsen layer, the Boltzmann–BGK equation is scaled in the normal direction to the walls by the mean free path λ , while the tangential directions are scaled by the geometric length scale L_c . Thus, all perturbations to the mass distribution function and its respective moments (represented by α), take the form

$$\alpha = \alpha_H + \alpha_K. \quad (2.13)$$

This yields two physically distinct equations to solve. The bulk flow quantities are represented by a subscript H , while the Knudsen layer corrections are denoted by a subscript K .

The surface geometry within the Knudsen layer is specified using the method of moving frame (Cartan 1977; Sone 2000). A local orthonormal coordinate system is chosen comprising two (principal) tangent vectors t_i^1 and t_i^2 (parametrized by χ_1 and χ_2 respectively) and an associated outward wall-normal n_i . The coordinate normal to a solid wall is denoted η , and is scaled by the mean free path λ . The wall curvature is chosen to be negative when its centre of curvature lies within the gas (Sone 1969, 1974). The surface thus satisfies the following geometric relations

(see Cartan 1977; Sone 2000; Ando 2011):

$$t_j^q \frac{\partial t_i^q}{\partial x_j} = -\kappa_q n_i - (-1)^q g_q t_i^{3-q}, \tag{2.14a}$$

$$t_j^q \frac{\partial t_i^{3-q}}{\partial x_j} = (-1)^q g_q t_i^q, \tag{2.14b}$$

$$t_j^q \frac{\partial n_i}{\partial x_j} = \kappa_q t_i^q, \tag{2.14c}$$

$$t_j^q \frac{\partial \kappa_q}{\partial x_j} = -g_q (\kappa_1 - \kappa_2), \tag{2.14d}$$

$$\kappa_{ij} = \kappa_1 t_i^1 t_j^1 + \kappa_2 t_i^2 t_j^2, \tag{2.14e}$$

$$\bar{\kappa} = \frac{\kappa_1 + \kappa_2}{2}, \tag{2.14f}$$

where the index q takes the values 1, 2, and the normal and geodesic curvatures are κ_q and g_q , respectively. The curvature tensor κ_{ij} is defined on the surface in terms of the normal curvatures and local tangents, whereas the mean curvature is $\bar{\kappa}$.

2.2. Boundary conditions

Solution to (2.9) is sought subject to classic diffuse reflection from rigid walls of arbitrary and smooth shape. The functional form of the mass distribution function for reflected particles is

$$F_b = \rho_b \left(\frac{1}{\sqrt{\pi} v_{mp}(T_b)} \right)^3 \exp \left(- \left[\frac{v_i - V_i}{v_{mp}(T_b)} \right]^2 \right), \tag{2.15}$$

where the subscript ‘ b ’ denotes values at the solid walls, and V_i is the velocity of the solid walls.

Zero net mass flux at the solid walls is also required. This immediately leads to the following results for the density of particles re-emitted from the walls and the usual no-penetration condition:

$$\rho_b = -2 \frac{\sqrt{\pi}}{v_{mp}(T_b)} \int_{(v_i - V_i) n_i < 0} (v_i - V_i) n_i F \, d\mathbf{v}, \tag{2.16a}$$

$$V_i n_i = \bar{v}_i n_i. \tag{2.16b}$$

Linearizing and scaling (2.15) and (2.16) then gives the required set of boundary conditions for particles reflected from the solid wall:

$$\phi_b = \sigma_b + 2V_i v_i + \left(v_i^2 - \frac{3}{2} \right) \tau_b, \tag{2.17a}$$

$$\sigma_b = \sqrt{\pi} V_i n_i - \frac{1}{2} \tau_b - 2\sqrt{\pi} \int_{-\infty}^{\infty} \int_{-\infty}^{\infty} \int_{-\infty}^0 \xi \phi E(v_i t_i^1, v_i t_i^2, \xi) \, d\xi \, d(v_i t_i^1) \, d(v_i t_i^2), \tag{2.17b}$$

$$V_i n_i = \bar{v}_i n_i, \tag{2.17c}$$

$$\xi = v_i n_i - V_i n_i. \tag{2.17d}$$

We have defined the normalized Gaussian E :

$$E(v_1, v_2, v_3) = \pi^{-3/2} \exp \left(-v_1^2 - v_2^2 - v_3^2 \right). \tag{2.18}$$

From (2.17), it then follows that outgoing particles from the solid walls satisfy the condition

$$\phi_{K,\xi \geq 0} \Big|_{\eta=0} = \phi_b - \phi_H. \tag{2.19}$$

In the outer region of the Knudsen layer, i.e. $\eta \rightarrow \infty$, we also require that the Knudsen layer correction decays to zero,

$$\lim_{\eta \rightarrow \infty} \phi_{K,\xi < 0} = 0. \tag{2.20}$$

Finally, all solid walls are considered rigid, as formalized by the condition of zero rate-of-strain,

$$\frac{\partial V_i}{\partial x_j} + \frac{\partial V_j}{\partial x_i} = 0. \tag{2.21}$$

This ensures the curvatures κ_s and g_s are constant and well-defined over the course of the motion.

2.3. System of equations and their solution

The mass distribution function is written as the sum of a bulk flow component and a Knudsen layer correction, as per (2.13). This leads to the following set of scaled governing equations:

$$-\frac{i}{2} \beta k^2 \phi_H + k v_i \frac{\partial \phi_H}{\partial x_i} - \beta k^2 a_i v_i = \sigma_H - \phi_H + 2\bar{v}_{H|i} v_i + \left(v_i^2 - \frac{3}{2} \right) \tau_H, \tag{2.22a}$$

$$-\frac{i}{2} \beta k^2 \phi_K + k \left(v_i t_i^1 t_j^1 \frac{\partial \phi_K}{\partial x_j} + v_i t_i^2 t_j^2 \frac{\partial \phi_K}{\partial x_j} \right) = \sigma_K - \phi_K - v_i n_i \frac{\partial \phi_K}{\partial \eta} + 2\bar{v}_{K|i} v_i + \left(v_i^2 - \frac{3}{2} \right) \tau_K. \tag{2.22b}$$

Here, a vertical line ‘|’ in the subscript is used to delineate between the indices of the tensor and other subscripts; this notation shall be used henceforth.

The corresponding boundary conditions are given in (2.19) and (2.20), and the scaled collisional invariants become

$$\begin{bmatrix} 0 \\ 0 \\ 0 \end{bmatrix} = \int_{-\infty}^{\infty} \begin{bmatrix} 1 \\ \mathbf{v} \\ \mathbf{v}^2 \end{bmatrix} \left(\sigma_A - \phi_A + 2\bar{v}_{A|i} v_i + \left(v_i^2 - \frac{3}{2} \right) \tau_A \right) E(\mathbf{v}) \, d\mathbf{v}, \tag{2.23}$$

while the moment equations are

$$\sigma_A = \int_{-\infty}^{\infty} \phi_A E(\mathbf{v}) \, d\mathbf{v}, \tag{2.24a}$$

$$\bar{v}_{A|i} = \int_{-\infty}^{\infty} v_i \phi_A E(\mathbf{v}) \, d\mathbf{v}, \tag{2.24b}$$

$$\frac{3}{2} \tau_A = \int_{-\infty}^{\infty} \left(v_i^2 - \frac{3}{2} \right) \phi_A E(\mathbf{v}) \, d\mathbf{v}, \tag{2.24c}$$

and the pressure is

$$P_A = \sigma_A + \tau_A. \tag{2.25}$$

We emphasize that all variables in (2.22)–(2.25) represent their scaled quantities. The subscript A in (2.23)–(2.25) takes the values H or K .

The scaled Knudsen number, k , is defined by

$$k = \frac{\sqrt{\pi}}{2} Kn, \quad (2.26)$$

and the Stokes number, β , is

$$\beta = \frac{\omega L_c^2}{v_{kin}(T_0)}. \quad (2.27)$$

The scaled Knudsen number k and frequency ratio, ω/ν , are small and are related by

$$\frac{\omega}{\nu} = \frac{1}{2} \beta k^2. \quad (2.28)$$

The scaled Knudsen number k simplifies the resulting analytical expressions, and is used henceforth. The kinematic viscosity, $v_{kin}(T_0)$, at temperature T_0 is related to the most probable speed and mean free path by

$$v_{kin}(T_0) = \frac{\sqrt{\pi}}{4} v_{mp}(T_0) \lambda. \quad (2.29)$$

3. Asymptotic formulae

In this section, we derive the required asymptotic formulae for the bulk flow and Knudsen layer corrections, in the limit of small scaled Knudsen number, i.e. $k \ll 1$. With the Stokes number β being a natural parameter of the problem, the decomposition in (2.28) ensures that the frequency ratio is always small in the asymptotic limit of infinitesimal scaled Knudsen number.

The mass distribution function and its moments appearing in the linearized Boltzmann–BGK equation (2.22), the collisional invariants (2.23), the moment equations (2.24), and the diffuse reflection, zero net mass flux and decay conditions (equations (2.17), (2.19) and (2.20)), are expanded asymptotically in the small parameter k , i.e.

$$\alpha = \sum_{n=0}^{\infty} \alpha^{(n)} k^n, \quad (3.1)$$

where α represents any of these dependent functions, and $\alpha^{(n)}$ is the n th component. Substituting (3.1) into the bulk flow equation in (2.22), and equating powers of k , produces the required set of relations for $\phi_H^{(n)}$ (we remind the reader that $\phi_H^{(n)}$ is the n th-order term in the k -expansion of ϕ_H); see (3.1). Enforcing the collisional conservation laws (equation (2.23)) produces a set of hydrodynamic equations at each order in k . These are analysed up to second order (i.e. $n = 2$) in § 3.1.

The corresponding boundary conditions at each order, n , are derived by analysis of the Knudsen layer equation in (2.22). This results in a set of first-order differential equations for $\phi_K^{(n)}$, i.e. the n th-order term in the k -expansion of ϕ_K . Substituting the solutions to these differential equations into the moment equations (2.24), yields a set of simultaneous integral equations. The integral equations at second order (i.e. $n = 2$) are given in appendix A – integral equations at lower order are identical to steady flow (Sone 1969), as we shall discuss. Solutions to the integral equations for $n \leq 2$ are obtained using numerical techniques and give the required bulk flow boundary conditions and Knudsen layer corrections.

3.1. *Hilbert expansion and bulk flow hydrodynamic equations*

Proceeding as outlined above, we arrive at the following results for $\phi_H^{(n)}$:

$$\phi_H^{(0)} = \sigma_H^{(0)} + 2\bar{v}_{H|i}^{(0)}v_i + \left(v_i^2 - \frac{3}{2}\right)\tau_H^{(0)}, \tag{3.2a}$$

$$\phi_H^{(1)} = \sigma_H^{(1)} + 2\bar{v}_{H|i}^{(1)}v_i + \left(v_i^2 - \frac{3}{2}\right)\tau_H^{(1)} - v_j \frac{\partial \phi_H^{(0)}}{\partial x_j}, \tag{3.2b}$$

$$\phi_H^{(2)} = \sigma_H^{(2)} + 2\bar{v}_{H|i}^{(2)}v_i + \left(v_i^2 - \frac{3}{2}\right)\tau_H^{(2)} - v_j \frac{\partial \phi_H^{(1)}}{\partial x_j} + \frac{i}{2}\beta\phi_H^{(0)} + \beta a_i v_i, \tag{3.2c}$$

$$\phi_H^{(n)} = \sigma_H^{(n)} + 2\bar{v}_{H|i}^{(n)}v_i + \left(v_i^2 - \frac{3}{2}\right)\tau_H^{(n)} - v_j \frac{\partial \phi_H^{(n-1)}}{\partial x_j} + \frac{i}{2}\beta\phi_H^{(n-2)}, \quad n \geq 3. \tag{3.2d}$$

Substituting (3.2) into the collision invariants in (2.23), and after some algebra, we obtain the required set of bulk flow hydrodynamic equations listed in table 1. Note that the order $n = 3$ continuity equation is required to close the order $n = 2$ hydrodynamic system (not shown).

The results in table 1 contrast with the steady formulation ($\beta = 0$) of Sone (1969), where it was found that the incompressible Stokes equations were recovered to all orders in the scaled Knudsen number k . Indeed, Sone’s steady results are recovered from table 1 for $\beta = 0$. For the general unsteady case, $\beta > 0$, gas compressibility affects the equations of motion for $n \geq 1$. Specifically, the linearized Navier–Stokes equations are recovered at leading order, with compressibility effects and temperature corrections modifying the bulk flow equations at higher order; the first-order equations were discussed in Sone (2000). Even for isothermal and unidirectional flows, unsteady effects lead to departures from the classical linearized Navier–Stokes equation at higher order ($n \geq 2$); see table 1.

3.2. *Knudsen layer corrections and boundary conditions*

Performing a similar analysis for the Knudsen layer leads to the following set of first-order governing equations for $\phi_K^{(n)}$:

$$v_i n_i \frac{\partial \phi_K^{(n)}}{\partial \eta} + \phi_K^{(n)} = Q^{(n)}, \tag{3.3}$$

where

$$Q^{(0)} = \sigma_K^{(0)} + 2\bar{v}_{K|i}^{(0)}v_i + \left(v_i^2 - \frac{3}{2}\right)\tau_K^{(0)}, \tag{3.4a}$$

$$Q^{(1)} = \sigma_K^{(1)} + 2\bar{v}_{K|i}^{(1)}v_i + \left(v_i^2 - \frac{3}{2}\right)\tau_K^{(1)} - v_i \left(\frac{\partial \chi_1}{\partial x_i} \frac{\partial \phi_K^{(0)}}{\partial \chi_1} + \frac{\partial \chi_2}{\partial x_i} \frac{\partial \phi_K^{(0)}}{\partial \chi_2}\right), \tag{3.4b}$$

$$Q^{(n)} = \sigma_K^{(n)} + 2\bar{v}_{K|i}^{(n)}v_i + \left(v_i^2 - \frac{3}{2}\right)\tau_K^{(n)} - v_i \left(\frac{\partial \chi_1}{\partial x_i} \frac{\partial \phi_K^{(n-1)}}{\partial \chi_1} + \frac{\partial \chi_2}{\partial x_i} \frac{\partial \phi_K^{(n-1)}}{\partial \chi_2}\right) + \frac{i}{2}\beta\phi_K^{(n-2)}, \quad n \geq 2. \tag{3.4c}$$

$n = 0$

$$0 = \frac{\partial P_H^{(0)}}{\partial x_i}$$

$$0 = \frac{\partial \bar{v}_{H|i}^{(0)}}{\partial x_i}$$

$$-i\beta \bar{v}_{H|i}^{(0)} = -\frac{\partial P_H^{(1)}}{\partial x_i} + \frac{\partial^2 \bar{v}_{H|i}^{(0)}}{\partial x_j^2} + \beta a_i$$

$$-\frac{3i}{5}\beta \left(\tau_H^{(0)} - \frac{2}{3}\sigma_H^{(0)} \right) = \frac{\partial^2 \tau_H^{(0)}}{\partial x_i^2}$$

$n = 1$

$$\frac{i}{2}\beta \sigma_H^{(0)} = \frac{\partial \bar{v}_{H|i}^{(1)}}{\partial x_i}$$

$$-i\beta \bar{v}_{H|i}^{(1)} = -\frac{\partial P_H^{(2)}}{\partial x_i} + \frac{\partial^2 \bar{v}_{H|i}^{(1)}}{\partial x_j^2} + \frac{1}{3} \frac{\partial^2 \bar{v}_{H|j}^{(1)}}{\partial x_i \partial x_j} + \frac{2i\beta}{3} \frac{\partial \tau_H^{(0)}}{\partial x_i}$$

$$-\frac{3i}{5}\beta \left(\tau_H^{(1)} - \frac{2}{3}\sigma_H^{(1)} \right) = \frac{\partial^2 \tau_H^{(1)}}{\partial x_i^2}$$

$n = 2$

$$\frac{i}{2}\beta \sigma_H^{(1)} = \frac{\partial \bar{v}_{H|i}^{(2)}}{\partial x_i}$$

$$-i\beta \bar{v}_{H|i}^{(2)} + \frac{\beta^2}{2} \bar{v}_{H|i}^{(0)} = -\frac{\partial P_H^{(3)}}{\partial x_i} + \frac{\partial^2 \bar{v}_{H|i}^{(2)}}{\partial x_j^2} + \frac{1}{3} \frac{\partial^2 \bar{v}_{H|j}^{(2)}}{\partial x_i \partial x_j} + \frac{2i\beta}{3} \frac{\partial \tau_H^{(1)}}{\partial x_i} - \frac{23i\beta}{30} \frac{\partial P_H^{(1)}}{\partial x_i}$$

$$-\frac{i}{2}\beta^2 a_i - \beta \left(\frac{\partial^2 a_i}{\partial x_j^2} + \frac{\partial^2 a_j}{\partial x_i \partial x_j} \right)$$

$$-\frac{3i}{5}\beta \left(\tau_H^{(2)} - \frac{2}{3}\sigma_H^{(2)} \right) - \frac{29i}{20}\beta \left(\frac{\partial^2 \tau_H^{(0)}}{\partial x_i^2} \right) = \frac{\partial^2 \tau_H^{(2)}}{\partial x_i^2} + \frac{19}{5} \frac{\partial^2}{\partial x_j^2} \left(\frac{\partial^2 \tau_H^{(0)}}{\partial x_i^2} \right)$$

TABLE 1. Bulk flow hydrodynamic equations up to and including second order.

The associated boundary conditions at order n are (equations (2.17), (2.19) and (2.20))

$$\phi_b^{(n)} = \sigma_b^{(n)} + 2V_i^{(n)} v_i + \left(v_i^2 - \frac{3}{2} \right) \tau_b^{(n)}, \tag{3.5a}$$

$$\sigma_b^{(n)} = \sqrt{\pi} V_i^{(n)} n_i - \frac{1}{2} \tau_b^{(n)} - 2\sqrt{\pi} \int_{-\infty}^{\infty} \int_{-\infty}^{\infty} \int_{-\infty}^0 \xi \phi^{(n)} E(v_i t_i^1, v_i t_i^2, \xi) d\xi d(v_i t_i^1) d(v_i t_i^2), \tag{3.5b}$$

$$V_i^{(n)} n_i = \bar{v}_i^{(n)} n_i. \tag{3.5c}$$

(a) Leading-order Knudsen layer corrections for the unsteady flow problem.

$$\begin{array}{ll}
 \left(\bar{v}_{H|i}^{(0)} - V_i^{(0)}\right) t_i^{1,2} & 0 \\
 \tau_H^{(0)} - \tau_b^{(0)} & 0 \\
 \left(\bar{v}_{H|i}^{(0)} - V_i^{(0)}\right) n_i & 0 \\
 \bar{v}_{K|i}^{(0),1,2} & 0 \\
 \bar{v}_{K|i}^{(0)} n_i & 0 \\
 \sigma_K^{(0)} & 0 \\
 \tau_K^{(0)} & 0
 \end{array}$$

(b) First-order Knudsen layer corrections for the unsteady flow problem.

$$\begin{array}{ll}
 \left(\bar{v}_{H|i}^{(1)} - V_i^{(1)}\right) t_i^{1,2} & k_0 S_{H|ij}^{(0)} n_i t_j^{1,2} + K_1 G_{H|i}^{(0)} t_i^{1,2} \\
 \tau_H^{(1)} - \tau_b^{(1)} & -d_1 G_{H|i}^{(0)} n_i \\
 \left(\bar{v}_{H|i}^{(1)} - V_i^{(1)}\right) n_i & 0 \\
 \bar{v}_{K|i}^{(1),1,2} & Y_0(\eta) S_{H|ij}^{(0)} n_i t_j^{1,2} + \frac{1}{2} Y_1(\eta) G_{H|i}^{(0)} t_i^{1,2} \\
 \bar{v}_{K|i}^{(1)} n_i & 0 \\
 \sigma_K^{(1)} & -\Omega_1(\eta) G_{H|i}^{(0)} n_i \\
 \tau_K^{(1)} & -\Theta_1(\eta) G_{H|i}^{(0)} n_i
 \end{array}$$

TABLE 2. Knudsen layer results for the unsteady flow problem up to first order. Slip coefficients and Knudsen layer corrections are summarized in appendix B.

Equation (3.3) can be solved subject to (3.5), yielding the required solutions for all n :

$$\phi_K^{(n)} = \begin{cases} \left(\phi_b^{(n)} - \phi_H^{(n)}\right) \exp\left(-\frac{\eta}{v_i n_i}\right) + \frac{1}{v_i n_i} \int_0^\eta Q^{(n)} \exp\left(-\frac{\eta - \eta_0}{v_i n_i}\right) d\eta_0, & v_i n_i \geq V_i n_i, \\ \frac{1}{v_i n_i} \int_\infty^\eta Q^{(n)} \exp\left(-\frac{\eta - \eta_0}{v_i n_i}\right) d\eta_0, & v_i n_i < V_i n_i. \end{cases} \tag{3.6}$$

3.2.1. *Leading- and first-order results*

Considering the cases of $n = 0, 1$, we substitute (3.6) into the moment (2.24). This enables the Knudsen layer corrections and associated boundary conditions for the bulk flow to be determined. A set of integral equations are derived and solved numerically using the refined moment method (Sone & Onishi 1973). This method will be outlined

shortly. The results of the analysis are given in table 2; all bulk flow quantities in table 2 are evaluated at the solid wall.

We have also defined $S_{H|ij}^{(n)}$ to be the rate-of-strain tensor, and $G_{H|i}^{(n)}$ the temperature gradient vector, each evaluated on the wall ($\eta = 0$),

$$S_{H|ij}^{(n)} = - \left(\frac{\partial \bar{v}_{H|i}^{(n)}}{\partial x_j} + \frac{\partial \bar{v}_{H|j}^{(n)}}{\partial x_i} \right), \quad G_{H|i}^{(n)} = - \frac{\partial \tau_H^{(n)}}{\partial x_i}. \quad (3.7)$$

Importantly, the quantities $\phi_H^{(0)}$, $\phi_H^{(1)}$, $Q^{(0)}$ and $Q^{(1)}$ that appear in (3.6) for $n = 0, 1$ are independent of the unsteady parameter β , i.e. the Stokes number. The leading- and first-order Knudsen layer integral equations thus remain unchanged from the steady analysis of Sone (1969), and are omitted for brevity. The boundary conditions for the bulk flow and Knudsen layer corrections, up to first order ($n \leq 1$), remain unaffected by oscillatory motion; see table 2. This conclusion is consistent with the observations of Sone (2007), who considered unsteady tangential motion of the wall, i.e. zero wall-normal velocity and body force.

The Knudsen layer functions and the slip coefficients are found via a refined moment method analysis of the Knudsen layer integral equations. Each Knudsen layer function for the density, temperature and mean tangential velocity, $\Omega_m(\eta)$, $\Theta_m(\eta)$ and $Y_m(\eta)$ respectively in table 2, are expanded in the truncated series

$$\Psi(\eta) = \sum_{n=0}^N c_n J_n(\eta), \quad (3.8)$$

where Ψ represents any of Ω_m , Θ_m or Y_m ; the subscript m distinguishes between the different Knudsen layer functions, the coefficients c_n are to be evaluated, N is a positive integer and $J_n(\eta)$ are Abramowitz functions (Abramowitz & Stegun 1965),

$$J_n(\eta) = \int_0^\infty t^n \exp\left(-\frac{\eta}{t} - t^2\right) dt. \quad (3.9)$$

Expanding Ω_m , Θ_m or Y_m as in (3.8), the solution of a coupled set of integral equations for the Knudsen layer corrections and bulk flow boundary conditions reduces to a matrix inversion problem for the coefficients c_n and the slip coefficients. Our results are given in appendix B, enabling each Knudsen layer function to be readily evaluated. The coefficients c_n and the slip coefficients are quoted to a suitably high number of significant figures to yield solutions of similar accuracy to those summarized in Sone (2000).

3.2.2. *Second-order results*

Derivation of the second-order results ($n = 2$) requires $\phi_K^{(2)}$, which from (3.6) is

$$\phi_K^{(2)} = \left\{ \begin{array}{l} \left[\sigma_b^{(2)} - \sigma_H^{(2)} + 2v_i \left(V_i^{(2)} - \bar{v}_{H|i}^{(2)} \right) + \left(v_i^2 - \frac{3}{2} \right) \left(\tau_b^{(2)} - \tau_H^{(2)} \right) \right. \\ \left. + v_j \frac{\partial}{\partial x_j} \left(\sigma_H^{(1)} + 2v_i \bar{v}_{H|i}^{(1)} + \left(v_i^2 - \frac{3}{2} \right) \tau_H^{(1)} \right) \right. \\ \left. - v_j v_k \frac{\partial^2}{\partial x_j \partial x_k} \left(\sigma_H^{(0)} + 2v_i \bar{v}_{H|i}^{(0)} + \left(v_i^2 - \frac{3}{2} \right) \tau_H^{(0)} \right) \right. \\ \left. - \frac{i}{2} \beta \left(\sigma_H^{(0)} + 2v_i \left(\bar{v}_{H|i}^{(0)} + a_i \right) + \left(v_i^2 - \frac{3}{2} \right) \tau_H^{(0)} \right) \right] \exp \left(-\frac{\eta}{v_i n_i} \right) \\ \left. + \frac{1}{v_i n_i} \int_0^\eta \left[\sigma_K^{(2)} + 2\bar{v}_{K|i}^{(2)} v_i + \left(v_i^2 - \frac{3}{2} \right) \tau_K^{(2)} \right. \right. \\ \left. \left. - v_i \left(\frac{\partial \chi_1}{\partial x_i} \frac{\partial}{\partial \chi_1} + \frac{\partial \chi_2}{\partial x_i} \frac{\partial}{\partial \chi_2} \right) \phi_K^{(1)} + \frac{i}{2} \beta \phi_K^{(0)} \right] \exp \left(-\frac{\eta - \eta_0}{v_i n_i} \right) d\eta_0 \right\} \quad v_i n_i \geq V_i n_i \\ \\ \left\{ \begin{array}{l} \frac{1}{v_i n_i} \int_\infty^\eta \left[\sigma_K^{(2)} + 2\bar{v}_{K|i}^{(2)} v_i + \left(v_i^2 - \frac{3}{2} \right) \tau_K^{(2)} \right. \\ \left. - v_i \left(\frac{\partial \chi_1}{\partial x_i} \frac{\partial}{\partial \chi_1} + \frac{\partial \chi_2}{\partial x_i} \frac{\partial}{\partial \chi_2} \right) \phi_K^{(1)} + \frac{i}{2} \beta \phi_K^{(0)} \right] \exp \left(-\frac{\eta - \eta_0}{v_i n_i} \right) d\eta_0 \right\} \quad v_i n_i < V_i n_i. \end{array} \right. \quad (3.10)$$

Three β -dependent terms appear in (3.10): two are proportional to $\phi_K^{(0)}$, which is uniquely zero; one is proportional to $\phi_H^{(0)}$, which is non-zero in general. This indicates that the second-order Knudsen layer corrections and associated boundary conditions for the bulk flow may be altered by oscillatory motion.

To evaluate these corrections and boundary conditions, we follow the procedure outlined in §3.2.1. The complete set of second-order integral equations is given in tables 4 and 5 of appendix A. Numerical solution using the refined moment method yields the formulae summarized in table 3. The slip coefficients, and the Knudsen layer correction coefficients, c_n , are summarized in tables 8–11 of appendix B. The well-known steady solution (Sone 2000) is recovered in the zero β limit, as required.

3.2.3. *Implications*

Two important conclusions immediately result from the formulae in tables 2 and 3.

- (i) The *tangential* velocity Knudsen layer correction and associated boundary condition for the bulk flow, up to and including second order ($n \leq 2$), are unaffected by unsteady motion (non-zero β), i.e. the steady result of Sone (1969) holds true for all β . This finding is consistent with Hadjiconstantinou (2005b), who observed that the steady second-order slip model provides good agreement with DSMC simulations for hard spheres. Our analysis provides rigorous mathematical justification for the use of the steady tangential velocity condition for unsteady BGK gas flows.
- (ii) Importantly, all other Knudsen layer corrections and associated boundary conditions are altered at second order ($n = 2$). These modifications are driven by unsteady gas compressibility effects, thermal gradients within the gas, and non-zero wall-normal velocities. A requirement of steady flow is zero wall-normal velocity (see Sone 1969).

$$\begin{aligned}
 & k_0 S_{Hij}^{(1)} n_i t_j^{1,2} - K_1 \frac{\partial \tau_b^{(1)}}{\partial x_i} t_i^{1,2} + a_1 \frac{\partial S_{Hij}^{(0)}}{\partial x_k} n_i t_j^{1,2} n_k \\
 & + a_2 \bar{\kappa} S_{Hij}^{(0)} n_i t_j^{1,2} + a_3 \kappa_{ij} S_{Hijk}^{(0)} n_k t_i^{1,2} \\
 & + a_4 \frac{\partial G_{Hi}^{(0)}}{\partial x_j} n_j t_i^{1,2} + a_5 \bar{\kappa} G_{Hi}^{(0)} t_i^{1,2} + a_6 \kappa_{ij} G_{Hij}^{(0)} t_i^{1,2} \\
 (\bar{v}_{Hi}^{(2)} - V_i^{(2)}) t_i^{1,2} & \\
 & \frac{1}{2} \left(\frac{\partial S_{Hij}^{(0)}}{\partial x_k} n_i n_j n_k + 2 \kappa_{ij} \kappa_{ji} V_k^{(0)} n_k + 2 \left(t_k^1 \frac{\partial}{\partial x_k} + g_2 \right) \left[t_j^1 \frac{\partial (V_i^{(0)} n_i)}{\partial x_j} \right] \right. \\
 (\bar{v}_{Hi}^{(2)} - V_i^{(2)}) n_i & \left. + 2 \left(t_k^2 \frac{\partial}{\partial x_k} - g_1 \right) \left[t_j^2 \frac{\partial (V_i^{(0)} n_i)}{\partial x_j} \right] \right) \int_0^\infty Y_0(\eta_0) d\eta_0 \\
 & + \frac{1}{2} \left(\frac{\partial G_{Hi}^{(0)}}{\partial x_k} n_i n_k - \frac{\partial G_{Hi}^{(0)}}{\partial x_i} + 2 \bar{\kappa} G_{Hi}^{(0)} n_i \right) \int_0^\infty Y_1(\eta_0) d\eta_0 \\
 \tau_H^{(2)} - \tau_b^{(2)} & - d_4 \frac{\partial S_{Hij}^{(0)}}{\partial x_k} n_i n_j n_k - d_8 \left(\kappa_{ij} \kappa_{ji} V_k^{(0)} n_k \right. \\
 & \left. + \left(t_k^1 \frac{\partial}{\partial x_k} + g_2 \right) \left[t_j^1 \frac{\partial (V_i^{(0)} n_i)}{\partial x_j} \right] + \left(t_k^2 \frac{\partial}{\partial x_k} - g_1 \right) \left[t_j^2 \frac{\partial (V_i^{(0)} n_i)}{\partial x_j} \right] \right) \\
 & - d_1 G_{Hi}^{(1)} n_i - d_5 \bar{\kappa} G_{Hi}^{(0)} n_i - d_9 \frac{\partial G_{Hi}^{(0)}}{\partial x_i} - d_{10} \frac{\partial \bar{v}_{Hi}^{(1)}}{\partial x_i} \\
 \bar{v}_{K|i}^{(2)} t_i^{1,2} & Y_0(\eta) S_{Hij}^{(1)} n_i t_j^{1,2} - \frac{1}{2} Y_1(\eta) \frac{\partial \tau_b^{(1)}}{\partial x_i} t_i^{1,2} + Y_{a1}(\eta) \frac{\partial S_{Hij}^{(0)}}{\partial x_k} n_i t_j^{1,2} n_k \\
 & + Y_{a2}(\eta) \bar{\kappa} S_{Hij}^{(0)} n_i t_j^{1,2} + Y_{a3}(\eta) \kappa_{ij} S_{Hijk}^{(0)} n_k t_i^{1,2} \\
 & + Y_{a5}(\eta) \bar{\kappa} G_{Hi}^{(0)} t_i^{1,2} + Y_{a6}(\eta) \kappa_{ij} G_{Hij}^{(0)} t_i^{1,2} \\
 \bar{v}_{K|i}^{(2)} n_i & \frac{1}{2} \left(\frac{\partial S_{Hij}^{(0)}}{\partial x_k} n_i n_j n_k + 2 \kappa_{ij} \kappa_{ji} V_k^{(0)} n_k + 2 \left(t_k^1 \frac{\partial}{\partial x_k} + g_2 \right) \left[t_j^1 \frac{\partial (V_i^{(0)} n_i)}{\partial x_j} \right] \right. \\
 & \left. + 2 \left(t_k^2 \frac{\partial}{\partial x_k} - g_1 \right) \left[t_j^2 \frac{\partial (V_i^{(0)} n_i)}{\partial x_j} \right] \right) \int_\infty^\eta Y_0(\eta_0) d\eta_0 \\
 & + \frac{1}{2} \left(\frac{\partial G_{Hi}^{(0)}}{\partial x_k} n_i n_k - \frac{\partial G_{Hi}^{(0)}}{\partial x_i} + 2 \bar{\kappa} G_{Hi}^{(0)} n_i \right) \int_\infty^\eta Y_1(\eta_0) d\eta_0
 \end{aligned}$$

TABLE 3. (Continued on next page)

(iii) The coefficient d_9 , which is given to 4 significant figures of accuracy in table 8, was also recently calculated by Takata *et al.* (2012). It is reported there as $\beta^{(2)}$, and is identical to our result to 4 significant figures.

$$\begin{aligned}
 \sigma_K^{(2)} & -\Omega_4(\eta) \frac{\partial S_{Hij}^{(0)}}{\partial x_k} n_i n_j n_k - \Omega_8(\eta) \left(\kappa_{ij} \kappa_{ji} V_k^{(0)} n_k \right. \\
 & \left. + \left(t_k^1 \frac{\partial}{\partial x_k} + g_2 \right) \left[t_j^1 \frac{\partial \left(V_i^{(0)} n_i \right)}{\partial x_j} \right] + \left(t_k^2 \frac{\partial}{\partial x_k} - g_1 \right) \left[t_j^2 \frac{\partial \left(V_i^{(0)} n_i \right)}{\partial x_j} \right] \right) \\
 & - \Omega_1(\eta) G_{Hi}^{(1)} n_i - \Omega_5(\eta) \bar{\kappa} G_{Hi}^{(0)} n_i - \Omega_9(\eta) \frac{\partial G_{Hi}^{(0)}}{\partial x_i} - \Omega_{10}(\eta) \frac{\partial \bar{v}_{Hi}^{(1)}}{\partial x_i} \\
 \tau_K^{(2)} & -\Theta_4(\eta) \frac{\partial S_{Hij}^{(0)}}{\partial x_k} n_i n_j n_k - \Theta_8(\eta) \left(\kappa_{ij} \kappa_{ji} V_k^{(0)} n_k \right. \\
 & \left. + \left(t_k^1 \frac{\partial}{\partial x_k} + g_2 \right) \left[t_j^1 \frac{\partial \left(V_i^{(0)} n_i \right)}{\partial x_j} \right] + \left(t_k^2 \frac{\partial}{\partial x_k} - g_1 \right) \left[t_j^2 \frac{\partial \left(V_i^{(0)} n_i \right)}{\partial x_j} \right] \right) \\
 & - \Theta_1(\eta) G_{Hi}^{(1)} n_i - \Theta_5(\eta) \bar{\kappa} G_{Hi}^{(0)} n_i - \Theta_9(\eta) \frac{\partial G_{Hi}^{(0)}}{\partial x_i} - \Theta_{10}(\eta) \frac{\partial \bar{v}_{Hi}^{(1)}}{\partial x_i}
 \end{aligned}$$

TABLE 3. Knudsen layer corrections for the unsteady flow problem at second order.

The formulae in tables 1–3 provide a complete asymptotic theory correct to $O(k^2)$, in the limit of small scaled Knudsen number, k , and small frequency ratio ω/ν . The associated slip coefficients, and the Knudsen layer coefficients c_n , are given in appendix B.

4. Application to time-varying thermal creep

In this section, we apply the theory developed in § 3 to study the flow generated by oscillatory (time-varying) temperature gradients imposed at two adjacent walls.

Consider two walls of infinite extent that are separated by a distance L ; see figure 1. A temperature gradient is applied along each wall in the x -direction. If the gas between the walls is permitted to relax thermally, steady flow results from the cold region to the hot region. This flow is commonly referred to as thermal creep (Kennard 1938; Maxwell 1879; Reynolds 1879; Sone 1966). If the ends of the channel are enclosed (the system is sealed), gradients in gas particle density that are created by thermal creep between the walls induce a pressure gradient. This generates a secondary Poiseuille flow (in the opposite direction) superimposed on the thermal creep flow: this is referred to as thermal transpiration (Ohwada *et al.* 1989*b*; Williams 1971).

We consider two cases: (i) temperature gradients at each wall are identical (referred to as the *symmetric* problem); and (ii) these temperature gradients are equal in magnitude but opposite in sign (the *antisymmetric* problem). A linear combination of these canonical flow problems enables the solution for arbitrary temperature gradients to be calculated.

From the governing bulk flow equations in table 1, it is evident that unsteady effects manifest themselves at first order for thermally driven flows. Consequently, both the symmetric and antisymmetric problems will be calculated correct to first order, i.e. $n \leq 1$.

Temperature gradients at the walls are in the x -direction, and are of magnitude A . The oscillation frequency is ω and the geometric length scale is the separation between

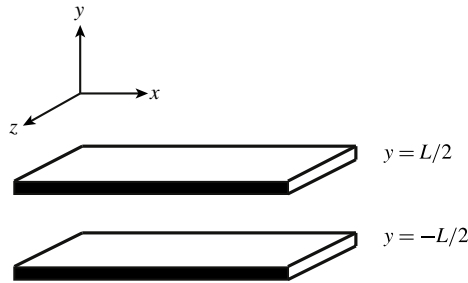


FIGURE 1. Schematic showing infinite parallel walls where temperature gradients are applied in the x -direction. Gas is confined between the walls.

the walls L . In accord with the above theory, the oscillation frequency ω is taken to be much smaller than the molecular collision frequency ν , and the wall separation L greatly exceeds the mean free path λ .

4.1. Symmetric problem

We first consider the symmetric case where temperature gradients at the walls are identical. Governing equations for the leading- and first-order mean velocity fields, $\bar{v}_{Hi}^{(0)}$ and $\bar{v}_{Hi}^{(1)}$, and temperature distributions, $\tau_H^{(0)}$ and $\tau_H^{(1)}$, are given in table 1, with associated boundary conditions in table 2. The flow is driven by the leading-order temperature boundary condition, which for this symmetric problem is

$$\tau_H^{(0)}|_{y=\pm L/2} = x\epsilon, \quad (4.1)$$

where $\epsilon \equiv AL/T_0$; T_0 is the equilibrium temperature of the gas. Solution to the resulting system at leading order yields the trivial result for the mean velocity,

$$\bar{v}_{Hi}^{(0)} = 0, \quad (4.2)$$

whereas the leading-order temperature distribution satisfies the classical heat diffusion equation, and is given by

$$\tau_H^{(0)} = x\epsilon \frac{\cosh(y\delta)}{\cosh\left(\frac{\delta}{2}\right)}, \quad (4.3)$$

with $\delta = \sqrt{-i\beta}$. The leading-order pressure is gradient-free, i.e. it is spatially invariant.

The first-order mean normal velocity at the walls is zero, in accord with the no-penetration condition, while the mean tangential velocity satisfies the slip boundary conditions (see table 2)

$$\bar{v}_{H|x}^{(1)}|_{y=\pm L/2} = -K_1\epsilon. \quad (4.4)$$

The slip at the walls is thus identical to the usual steady problem.

The first-order mean velocity is calculated by seeking a solution of the form

$$\bar{v}_{H|x}^{(1)} = -\frac{x^2}{2}g'(y) + h(y), \quad (4.5a)$$

$$\bar{v}_{H|y}^{(1)} = xg(y) + xf(y), \quad (4.5b)$$

where the functions $g(y)$, $f(y)$ and $h(y)$ are to be determined. The first terms in $\bar{v}_{H|x}^{(1)}$ and $\bar{v}_{H|y}^{(1)}$ provide a divergence-free contribution to the velocity field. The function $xf(y)$ is chosen to ensure that the divergence of the velocity field varies linearly in x (see table 1 and (4.3)), whereas $h(y)$ is included for generality.

Substituting (4.5) into the first-order continuity and momentum equations in table 1, and applying the associated boundary conditions, leads to the unique solution

$$g(y) = -\frac{\delta\epsilon \tanh\left(\frac{\delta}{2}\right)}{\delta \cosh\left(\frac{\delta}{2}\right) - 2 \sinh\left(\frac{\delta}{2}\right)} \left[\left(y - \frac{1}{2}\right) \delta \cosh\left(\frac{\delta}{2}\right) + \left(\sinh\left(\frac{\delta}{2}\right) - \sinh(y\delta)\right) \right], \quad (4.6a)$$

$$h(y) = \frac{\epsilon}{8 \left[\delta \cosh\left(\frac{\delta}{2}\right) - 2 \sinh\left(\frac{\delta}{2}\right) \right]} \left[2y\delta \operatorname{sech}\left(\frac{\delta}{2}\right) \left(2 \sinh\left(\frac{\delta}{2}\right) \sinh(y\delta) - y\delta \sinh(\delta) \right) + \cosh(y\delta) \left(\delta - 2 \tanh\left(\frac{\delta}{2}\right) \right) \left(\delta \tanh\left(\frac{\delta}{2}\right) - 8K_1 \right) \right], \quad (4.6b)$$

$$f(y) = \frac{\delta\epsilon}{2} \left[\frac{\sinh(\delta y) - \sinh\left(\frac{\delta}{2}\right)}{\cosh\left(\frac{\delta}{2}\right)} \right], \quad (4.6c)$$

where the slip coefficient $K_1 = -0.383161\dots < 0$. This yields the required mean velocity field, pressure and temperature distributions at first order ($n = 1$):

$$P_H^{(1)} = C, \quad (4.7a)$$

$$\tau_H^{(1)} = -xd_1\epsilon\delta \tanh\left(\frac{\delta}{2}\right) \frac{\cosh(y\delta)}{\cosh\left(\frac{\delta}{2}\right)} + \frac{2}{5}C \left(1 - \frac{\cosh(y\delta)}{\cosh\left(\frac{\delta}{2}\right)} \right), \quad (4.7b)$$

$$\bar{v}_{H|y}^{(1)} = x\delta^2\epsilon \frac{\sinh(y\delta) - 2y \sinh\left(\frac{\delta}{2}\right)}{2\delta \cosh\left(\frac{\delta}{2}\right) - 4 \sinh\left(\frac{\delta}{2}\right)}, \quad (4.7c)$$

$$\begin{aligned} \bar{v}_{H|x}^{(1)} = & -\epsilon K_1 \frac{\cosh(y\delta)}{\cosh\left(\frac{\delta}{2}\right)} + \frac{\epsilon}{2\delta \cosh\left(\frac{\delta}{2}\right) - 4 \sinh\left(\frac{\delta}{2}\right)} \\ & \times \left(x^2\delta^2 \tanh\left(\frac{\delta}{2}\right) \left[\cosh\left(\frac{\delta}{2}\right) - \cosh(y\delta) \right] \right. \\ & \left. + \frac{\delta \cosh(y\delta)}{4} \left[2\operatorname{sech}^2\left(\frac{\delta}{2}\right) - 2 + \delta \tanh\left(\frac{\delta}{2}\right) \right] \right) \end{aligned}$$

$$+ \tanh\left(\frac{\delta}{2}\right) \left[y \sinh\left(\frac{\delta}{2}\right) - y^2 \delta \cosh\left(\frac{\delta}{2}\right) \right], \quad (4.7d)$$

$$P_H^{(2)} = \frac{x\delta^2\epsilon}{2\delta \cosh\left(\frac{\delta}{2}\right) - 4 \sinh\left(\frac{\delta}{2}\right)} \left[y^2 \delta^2 \sinh\left(\frac{\delta}{2}\right) - \frac{x^2 \delta^2}{3} \sinh\left(\frac{\delta}{2}\right) \right. \\ \left. + \cosh(y\delta) \left(2 \tanh\left(\frac{\delta}{2}\right) - \delta \right) \right] + D. \quad (4.7e)$$

Note that closure of the leading-order pressure $P_H^{(0)}$ is achieved at first order, and gives $P_H^{(0)} = 0$. The constants C and D in the first- and second-order pressures can also be evaluated at subsequent order, i.e. $n = 2$ and 3 , respectively.

The corresponding Knudsen layer corrections are then obtained by substituting (4.2) and (4.3) into table 2,

$$\tau_k^{(1)} = -x\delta\epsilon \tanh\left(\frac{\delta}{2}\right) \left[\Theta_1\left(\frac{\frac{1}{2} - y}{k}\right) + \Theta_1\left(\frac{\frac{1}{2} + y}{k}\right) \right], \quad (4.8a)$$

$$\bar{v}_{k|x}^{(1)} = -\frac{\epsilon}{2} \left[Y_1\left(\frac{\frac{1}{2} - y}{k}\right) + Y_1\left(\frac{\frac{1}{2} + y}{k}\right) \right], \quad (4.8b)$$

where the functions $\Theta_1(\eta)$ and $Y_1(\eta)$ are defined in (3.8), with associated coefficients c_n given in appendix B.

Interestingly, the spatial dependence of the tangential velocity correction, $\bar{v}_{k|x}^{(1)}$, is independent of the oscillation frequency, i.e. independent of β . As such, it is identical to the corresponding result for steady flow; see Sone (2000). To explicate the effect of unsteadiness on classical thermal creep flow, we thus focus our analysis on the bulk flow results in (4.2), (4.3) and (4.7). Together with (4.8), these give the complete solution to $O(k)$.

4.1.1. Physical analysis of the flow

To study the flow, plots of the real and imaginary components and the magnitude of $\tau_H^{(0)}/(x\epsilon)$ are given in figure 2. Note that the true (physical) solution of this time-varying flow is given by a weighted superposition between the real and imaginary components. For example, if the true temperature at the wall is $T_{true} = \text{Re}\{T \exp(-i\omega t)\}$, then all true flow/temperature variables are given by $X_{true} = \text{Re}\{X \exp(-i\omega t)\} = \text{Re}\{X\} \cos(\omega t) - \text{Im}\{X\} \sin(\omega t)$, for any variable X . Thus, the solution periodically alternates between the real and imaginary components, as time evolves.

In the limit of infinitesimal β , the temperature distribution is purely real and coincides with the steady solution of Sone (1966). The temperature distribution thus precisely follows the time variation in the wall temperature, i.e. it is in phase. From figure 2, it is clear that as β increases, a non-zero imaginary component arises representing a time lag in the gas temperature response. For large β , thermal boundary layers form in the immediate vicinity of the walls, where gas temperature variations are confined. Exponential decay in the temperature is observed away from the walls.

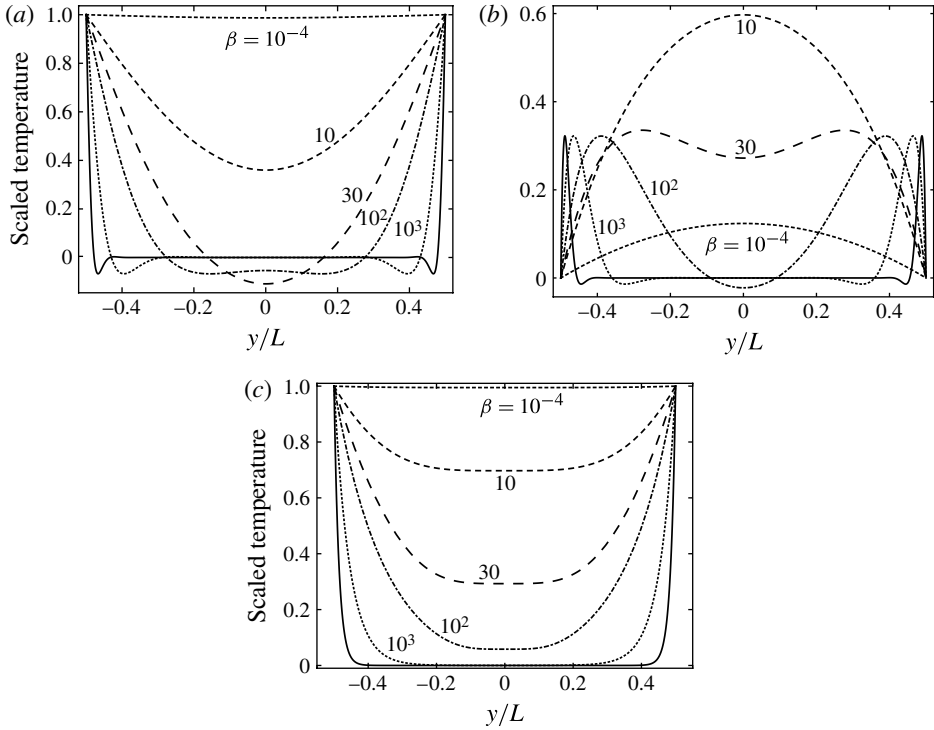


FIGURE 2. Scaled leading-order temperature perturbation of symmetric problem $\tau_H^{(0)}/(x\epsilon)$. (a) Real component; (b) imaginary component; (c) magnitude. Results given for $\beta = 1$ (short dashes), $\beta = 10$ (medium dashes), $\beta = 30$ (long dashes), $\beta = 100$ (dot-dashed line), $\beta = 1000$ (dotted line), $\beta = 10000$ (solid line).

Next, we calculate the average velocity u_y normal to the walls, in the upper half-channel,

$$u_y = 2 \int_0^{1/2} \bar{v}_{H|y}^{(1)} dy = -x\delta\epsilon \frac{\delta \sinh\left(\frac{\delta}{2}\right) - 8\sinh^2\left(\frac{\delta}{4}\right)}{4 \left[\delta \cosh\left(\frac{\delta}{2}\right) - 2 \sinh\left(\frac{\delta}{2}\right) \right]}. \tag{4.9}$$

Note that the normal velocity $\bar{v}_{H|y}^{(1)}$ is antisymmetric in y . The small- and large- β asymptotics of u_y are

$$u_y = x\epsilon \begin{cases} \frac{i\beta}{32} - \frac{\beta^2}{3840}, & \beta \ll 1, \\ \frac{-1 + i}{4} \sqrt{\frac{\beta}{2}} + \frac{1}{2}, & \beta \gg 1. \end{cases} \tag{4.10}$$

Comparison of the full solution in (4.9) and the asymptotic formulae in (4.10) is given in figure 3, where excellent agreement is observed.

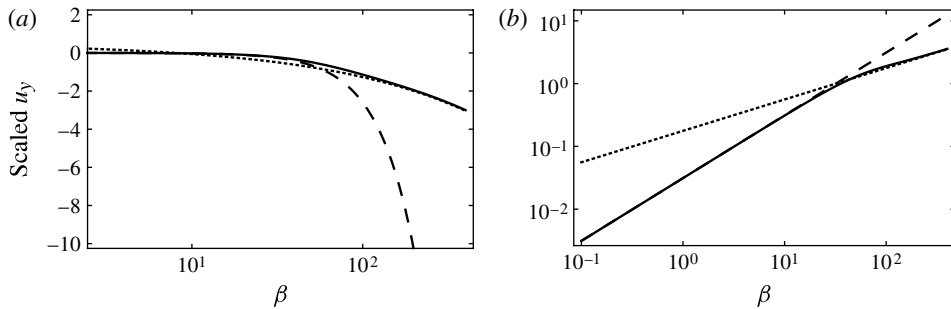


FIGURE 3. Scaled average normal velocity of symmetric problem $u_y/(x\epsilon)$. (a) Real component; (b) imaginary component. Exact solution, equation (4.9) (solid line). Asymptotic solutions, equation (4.10): $\beta \ll 1$ (long dashes); $\beta \gg 1$ (dotted line).

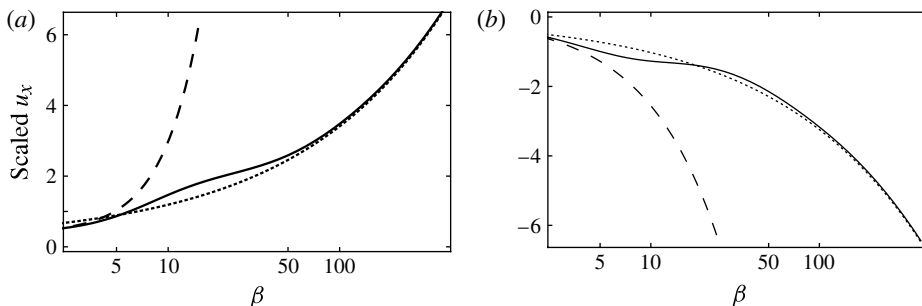


FIGURE 4. Scaled average tangential velocity of symmetric problem u_x/ϵ at $x = 1$. (a) Real component; (b) imaginary component. Exact solution, equation (4.11) (solid line). Asymptotic solutions, equation (4.12): $\beta \ll 1$ (long dashes); $\beta \gg 1$ (dotted line).

The corresponding average tangential velocity u_x is given by

$$u_x = \frac{\epsilon \operatorname{sech}\left(\frac{\delta}{2}\right) \tanh\left(\frac{\delta}{2}\right)}{48\delta \left[\delta \cosh\left(\frac{\delta}{2}\right) - 2 \sinh\left(\frac{\delta}{2}\right)\right]} \left(\delta [24 - (48K_1 + \delta^2 [1 - 12x^2]) (1 + \cosh(\delta))] \right) + 6 [16K_1 - 4 + (1 - 4x^2)] \sinh(\delta). \quad (4.11)$$

The asymptotic results for this expression are

$$u_x = \epsilon \begin{cases} -K_1 - \frac{i\beta}{240} (9 + 20K_1 + 60x^2) + \frac{\beta^2}{33600} (279 + 280K_1 + 700x^2), & \beta \ll 1, \\ \frac{-1 + i}{24} \sqrt{\frac{\beta}{2}} (1 - 12x^2) + \frac{1}{6}, & \beta \gg 1, \end{cases} \quad (4.12)$$

where the slip coefficient $K_1 = -0.383161\dots < 0$. Once more, comparison of (4.11) and (4.12) in figure 4 shows excellent agreement between the full solution and the corresponding low and high inertia asymptotics.

We now explore the physical mechanisms driving the thermal creep flow in the zero, small, intermediate and high inertia limits. These observations are then reconciled with the asymptotic forms of the average velocity as inertia is increased; see (4.10) and (4.12), and the corresponding mean velocities in the gas, $\bar{v}_{H|y}^{(1)}$ and $\bar{v}_{H|x}^{(1)}$, in (4.6).

Zero inertia ($\beta = 0$). In the limit of zero inertia, temperature gradients at the wall generate a velocity slip given in (4.4), and thus a thermal creep in the tangential direction to the walls (Sone 1966). This gives the first term in u_x for $\beta \ll 1$ in (4.12), with the corresponding mean velocity

$$\bar{v}_{H|x,sym}^{(1)} = -K_1\epsilon, \quad \bar{v}_{H|y,sym}^{(1)} = 0, \tag{4.13}$$

where the subscript ‘sym’ is used to identify this as the symmetric solution for zero inertia.

Small inertia ($\beta \ll 1$). In the limit of small inertia, the oscillatory (time-varying) pressure, temperature and density perturbations all drive a mean flow, in addition to the usual thermal creep (at zero inertia). This additional flow is out of phase with the thermal creep by 90° , which is evident from the small- β asymptotics in (4.10) and (4.12). Near the reference point of zero temperature ($x = 0$), gas compressibility is negligible, leading to a divergence-free velocity field. This directly leads to the $O(\beta)$ component in the average tangential velocity u_x that is independent of x ; see (4.12). Away from this point, gas compressibility becomes significant and introduces an additional term that is proportional to x^2 in u_x .

Plots of the mean normal velocity $\bar{v}_{H|y}^{(1)}$ at low inertia are given in figure 5. From (4.13), the steady mean normal velocity is zero, and thus the solution in (4.7) is directly driven by unsteady effects. The solution is proportional to x , and is appropriately scaled in figure 5 for simplicity. These results highlight the no-penetration condition at the walls. They also demonstrate that the low- β asymptotic solution for u_y holds over a wide range of values, $\beta \lesssim 30$.

Corresponding plots for the tangential component $\bar{v}_{H|x}^{(1)}$ are given in figure 6. To identify contributions from unsteady motion of the walls, results are given for the difference between $\bar{v}_{H|x}^{(1)}$ and the classical thermal creep solution from (4.13): this is termed the *unsteady correction*. The unsteady correction must satisfy no-slip at the walls; this is because slip along the walls is independent of β (see (4.4)). We now examine the nature of the flow and its dominant mechanism, as a function of inertia β and position x along the channel. We remind the reader that the classical thermal creep solution in (4.13) is purely real.

First, consider flow near the reference point at $x = 0$. Gradients in the pressure $P_H^{(2)}$ and the temperature $\tau_H^{(0)}$ are both capable of driving the flow. For small β , the tangential pressure gradient between the walls is given by

$$\frac{\partial P_{H2}}{\partial x} = \frac{i\beta\epsilon}{2} (1 + 6x^2 - 6y^2) + \frac{\beta^2\epsilon}{80} (-5 + 4x^2 + 16y^2), \tag{4.14}$$

whereas the tangential temperature gradient is

$$\frac{\partial \tau_{H0}}{\partial x} = \epsilon - \frac{i\beta\epsilon}{8} (4y^2 - 1) - \frac{\beta^2\epsilon}{384} (16y^4 - 24y^2 - 5). \tag{4.15}$$

For small β , this temperature gradient is constant to leading order. Coupled with the no-slip condition, this directly leads to the parabolic profile observed in the real component of the unsteady correction for $\beta = 10^{-4}$ at $x = 0$; see figure 6(a). The imaginary component, however, exhibits significantly different behaviour. Interestingly,

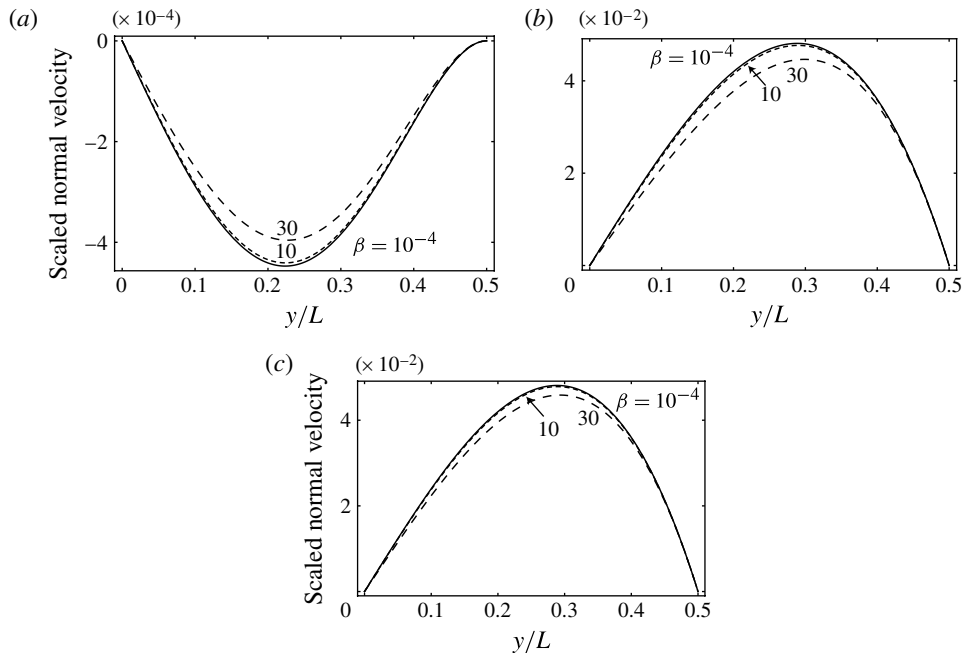


FIGURE 5. Scaled mean normal velocity of symmetric problem $\bar{v}_{H|y}^{(1)}/(x\beta^l\epsilon)$, where l is chosen to match dominant asymptotic behaviour in β . Real ($l = 2$), imaginary and magnitude ($l = 1$). (a) Real component; (b) imaginary component; (c) magnitude. Results given for $\beta = 10^{-4}$ (solid line), $\beta = 10$ (medium dashes), $\beta = 30$ (long dashes).

the pressure gradient varies quadratically with the normal coordinate y , and switches sign across the channel, i.e. as y is varied. This pressure gradient directly drives the imaginary component of the flow, and combined with the no-slip condition at the walls, leads to the observed variations in convexity in the imaginary component of the unsteady correction to $\bar{v}_{H|x}^{(1)}$, at low β ; see figure 6(b) for $\beta = 10^{-4}$. Since the classical thermal creep is purely real, the imaginary component of the unsteady correction to the mean tangential velocity is identical to the imaginary component of the complete bulk mean tangential velocity $\bar{v}_{H|x}^{(1)}$.

The imaginary component of $\bar{v}_{H|x}^{(1)}$ at $x = 0$ also vanishes twice at finite distance from the walls. Since the mean normal velocity $\bar{v}_{H|y}^{(1)}$ is proportional to x , this ensures that two critical points (saddle nodes) exist in the imaginary component of the velocity field at finite distance from the walls, at $x = 0$. For $\beta = 10^{-4}$, they occur at the points $(x, y) = (0, \pm y_c)$, where

$$y_c = 0.341817\dots \quad (4.16)$$

The extensional flow leading to this critical point is evident in the streamline plot of the complete bulk flow in figure 7(b), and highlighted in figure 8. We note that the complete bulk flow is the sum of the classical thermal creep in (4.13), and the unsteady correction. All streamlines presented in this article are streamlines of the complete flow.

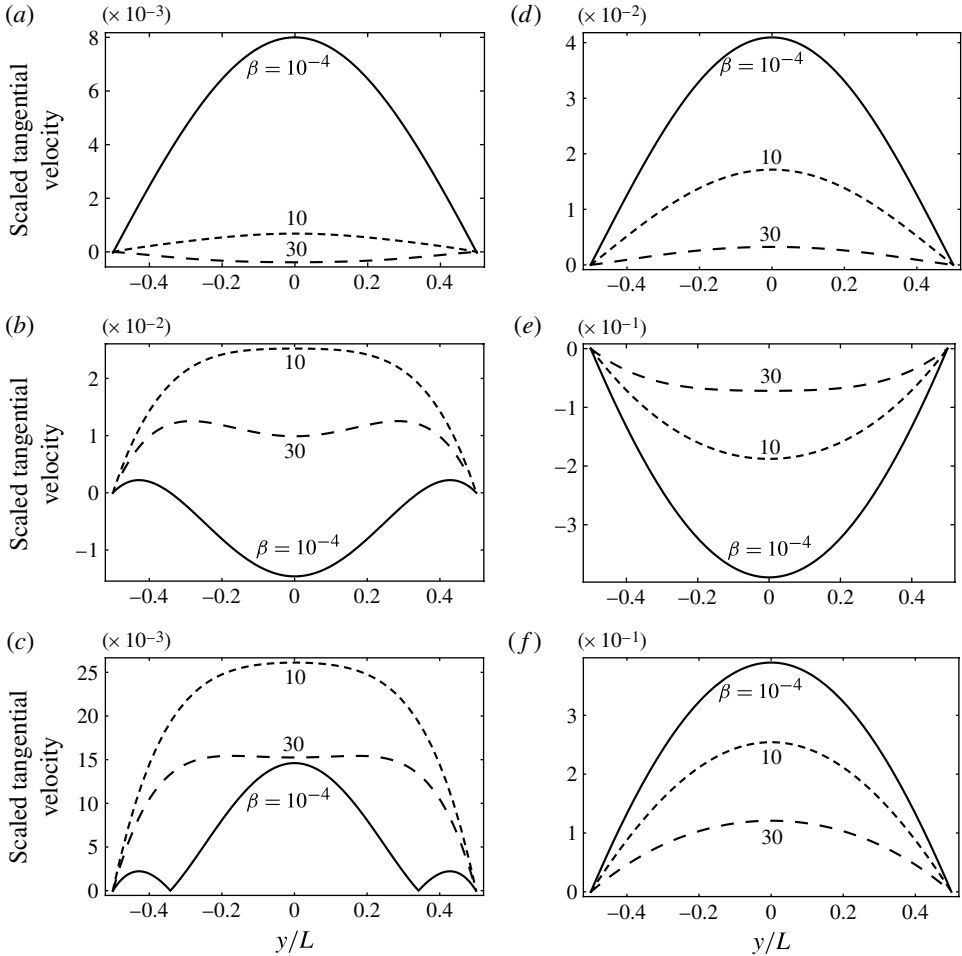


FIGURE 6. Scaled unsteady correction to the mean tangential velocity of symmetric problem $(\bar{v}_{H|x}^{(1)} - \bar{v}_{H|x, sym}^{(1)})/(\beta^l \epsilon)$, where l is chosen to match dominant asymptotic behaviour in β . Real ($l = 2$); imaginary and magnitude ($l = 1$). At $x = 0$: (a) real component; (b) imaginary component; (c) magnitude. At $x = 1$: (d) real component, (e) imaginary component; (f) magnitude. Results given for $\beta = 10^{-4}$ (solid line), $\beta = 10$ (medium dashes), $\beta = 30$ (long dashes).

Away from the reference point at $x = 0$, the pressure gradient grows in x and dominates the temperature gradient which is independent of x ; see (4.14) and (4.15). For large x , the pressure gradient is independent of y to leading order, and together with the no-slip condition, drives a parabolic flow; see figure 6(d–f) for $\beta = 10^{-4}$.

Intermediate inertia ($\beta \sim 1$). As β increases, the real component of the temperature gradient decreases; see real components of (4.15). This leads to a reduction in the real component of the unsteady correction to the tangential velocity; see figure 6(a) for $\beta = 10$. The opposite behaviour is observed for the imaginary component, with the temperature gradient increasing. This alters the convexity of the imaginary component of $\bar{v}_{H|x}^{(1)}$, as illustrated in figure 6(b) for $\beta = 10$, and extinguishes the critical points that were observed for low β .

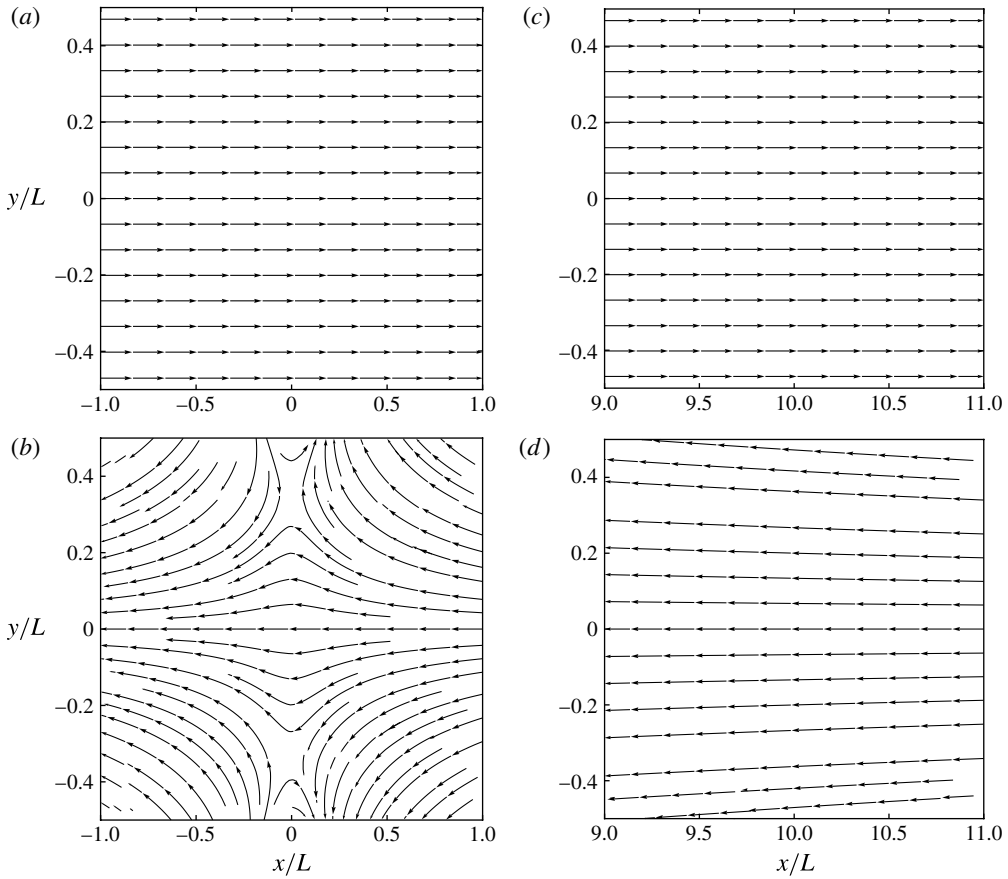


FIGURE 7. Streamlines of symmetric problem for $\beta = 10^{-4}$. Flow centred at $x = 0$: (a) real; (b) imaginary. Flow centred at $x = 10$: (c) real; (d) imaginary.

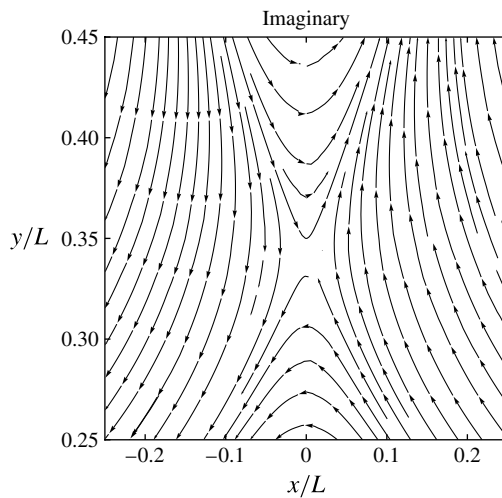


FIGURE 8. Streamlines of symmetric problem for $\beta = 10^{-4}$. Flow centred at $x = 0$. Zoomed image of figure 7(b) for $-0.25 \leq x/L \leq 0.25$ and $0.25 \leq y/L \leq 0.45$.

As β increases further, both real and imaginary components of the temperature and pressure gradients begin to balance. This inflects the unsteady correction to the velocity profile at $x = 0$; see figure 6(a–c) for $\beta = 30$. For $\beta > 30$, the real components of the temperature and pressure gradients identically oppose the classical thermal creep flow at the origin $(x, y) = (0, 0)$, which results in the formation of a critical point in the real component of $\bar{v}_{H|x}^{(1)}$, when the unsteady parameter β equals the critical value

$$\beta_c = 34.0487 \dots \quad (4.17)$$

This critical point then bifurcates to yield two symmetric critical points (centres) about $y = 0$ in the real component of the mean velocity, for higher β . This behaviour is illustrated in the streamlines of the complete bulk flow in figure 9(a) for $\beta = 50 > \beta_c$. Consequently, the nature of these points is distinct from that observed in the imaginary component for small β . The position of the critical point in the upper half-channel ($y > 0$) as a function of β is given in figure 10. The classical thermal creep flow is purely real. Hence, the formation of a critical point in the imaginary components of the mean velocity only requires the pressure and temperature gradients to balance. For intermediate β , these two effects do not exactly balance, and thus no critical points are observed in the imaginary component of the mean velocity for $\beta = 50$, except at the walls, due to the no-slip condition.

Away from the reference point at $x = 0$, similar flow profiles to those observed for $\beta = 10^{-4}$ are observed at intermediate inertia; see figure 6(d–f) for $\beta = 10$ and $\beta = 30$. In addition to the large pressure gradient for non-zero x , compressibility effects are significant with increasing β , leading to convergence of the streamlines for $x \gg 1$; see figure 9(c–d).

High inertia ($\beta \gg 1$). In the high inertia limit, perturbations to the temperature are confined to thin boundary layers near the walls; see figure 2. This produces large pressure gradients within the boundary layers, which dominate the flow and drive strong variations in the velocity fields near the walls; see figures 11 and 12. Perturbations to the gas temperature $\tau_H^{(0)}$, and hence density $\sigma_H^{(0)}$, decay exponentially away from the walls. This results in an incompressible flow for all x outside the boundary layers; see the $n = 1$ continuity equation in table 1. Pressure gradients remain significant outside the boundary layers and are thus the dominant force driving the bulk flow.

The normal mean velocity $\bar{v}_{H|y}^{(1)}$, plotted in figure 11, displays a linear dependence on the normal coordinate y . This is consistent with the large β asymptotic result for the pressure,

$$\frac{\partial P_H^{(2)}}{\partial y} = \sqrt{i}\beta^{3/2}\epsilon xy, \quad (4.18)$$

which is also proportional to y . Recall that the classical thermal creep solution has no normal component to the walls, and thus the results in figure 11 are identical to the unsteady correction.

In contrast, the unsteady correction to the mean tangential velocity $\bar{v}_{H|x}^{(1)}$ in figure 12 exhibits: (i) a parabolic distribution outside the boundary layers near the reference point $x = 0$; and (ii) plug flow away from this point (e.g. at $x = 1$). These features are also reconciled with the high- β asymptotic for the tangential pressure gradient:

$$\frac{\partial P_H^{(2)}}{\partial x} = \frac{\sqrt{i}\beta^{3/2}\epsilon}{2} (y^2 - x^2). \quad (4.19)$$

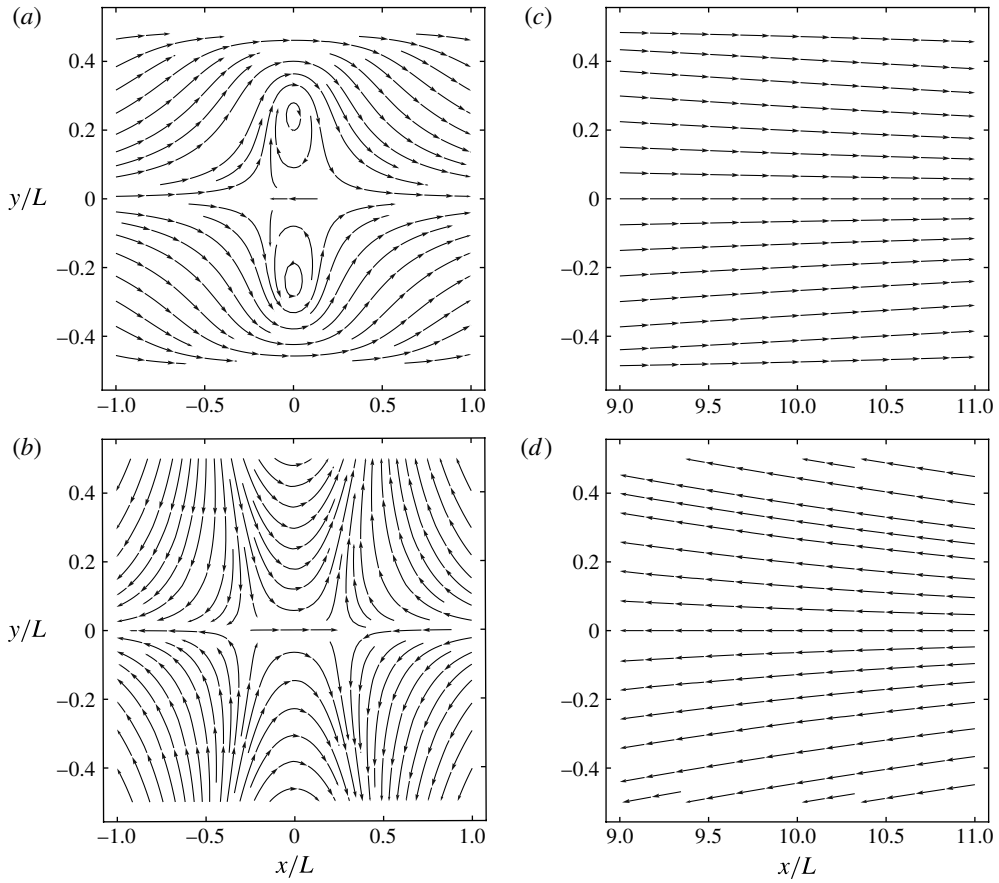


FIGURE 9. Streamlines of symmetric problem for $\beta = 50$. Flow centred at $x = 0$: (a) real; (b) imaginary. Flow centred at $x = 10$: (c) real; (d) imaginary.

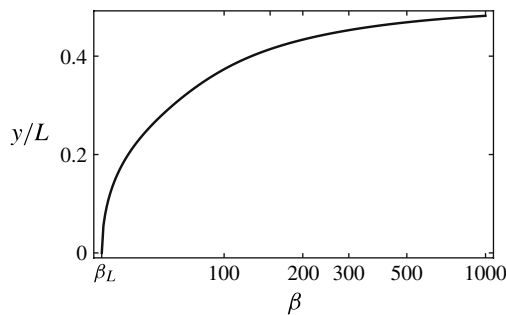


FIGURE 10. Position in the upper half-channel ($0 < y < 0.5$) of the critical point at $x = 0$ in the real mean tangential velocity of symmetric problem $\bar{v}_{H|x}^{(1)}$. Position given as a function of β .

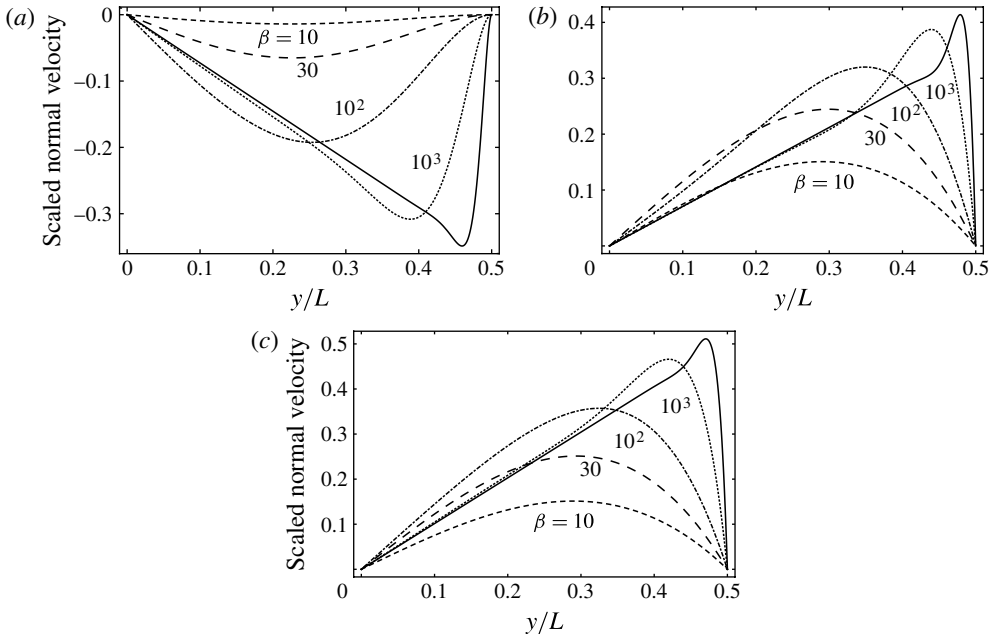


FIGURE 11. Scaled mean normal velocity of symmetric problem $\bar{v}_{Hy}^{(1)}/(x\sqrt{\beta}\epsilon)$. (a) Real component; (b) imaginary component; (c) magnitude. Results given for $\beta = 10$ (medium dashes), $\beta = 30$ (long dashes), $\beta = 100$ (dot-dashed line), $\beta = 1000$ (dotted line), $\beta = 10000$ (solid line).

This pressure gradient is dominated by a quadratic variation in y near the reference point ($x = 0$), leading to the observed parabolic velocity distribution in this incompressible flow; see figure 12(a–c). However, away from the reference point the quadratic variation in x dominates and thus reverses the sign of the pressure gradient. Since flow outside the boundary layers is always incompressible at high inertia (see above), this feature leads to plug flow in the opposite direction to the parabolic flow observed near the reference point; see figure 12(d–f).

Streamlines of the complete bulk flow are illustrated in figure 13 at two points along the walls, $x = 0$ and $x = 10$. The two critical points observed at intermediate inertia in the real component of the mean velocity (see figure 9) approach the walls as β increases. For high β , these critical points exist within the thermal boundary layers at the walls: these are not visible within the resolution of the plots in figure 13(a). No other critical points exist in the flow for finite β .

4.2. Antisymmetric problem

Next, we examine the antisymmetric case where temperature gradients at the walls are equal in magnitude but opposite in sign. We now set $\tau_H^{(0)}$ on the lower plate to be opposite in sign to that on the upper plate,

$$\tau_H^{(0)}|_{y=\pm 1/2} = \pm x\epsilon, \tag{4.20}$$

where $\epsilon \equiv AL/T_0$ and T_0 is the equilibrium temperature of the gas, as before.

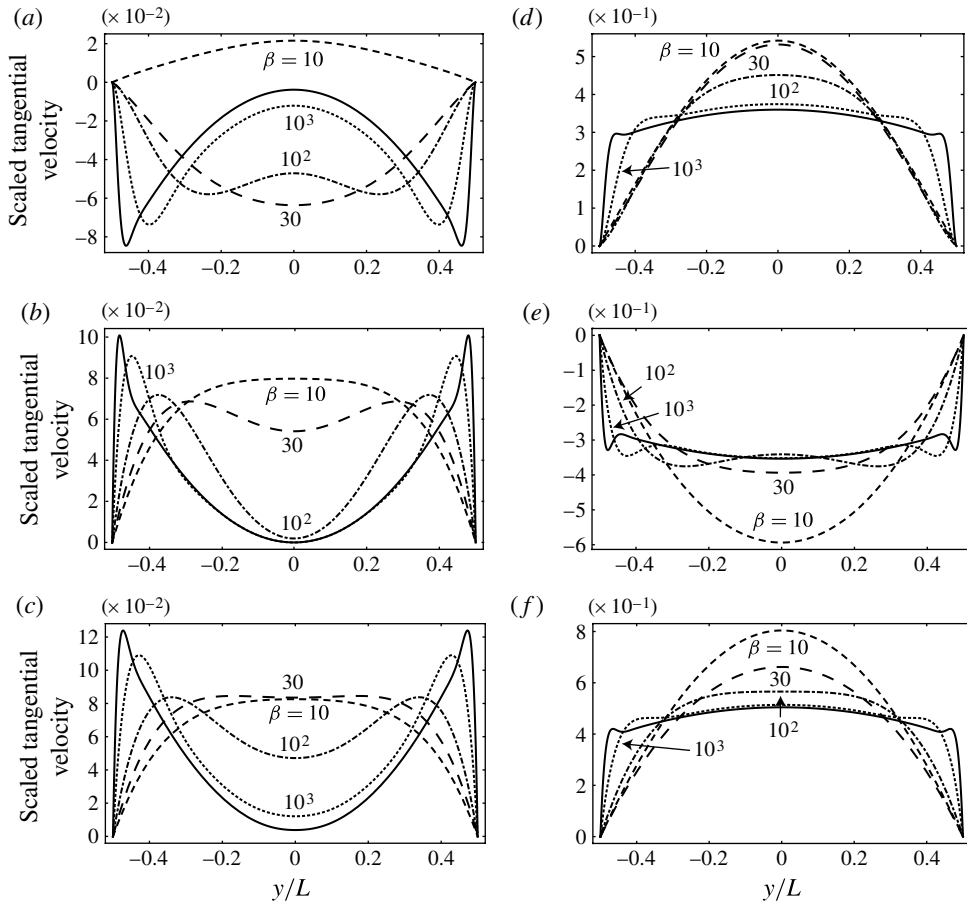


FIGURE 12. Scaled unsteady correction to mean tangential velocity of symmetric problem $(\bar{v}_{H|x}^{(1)} - \bar{v}_{H|x,\text{sym}}^{(1)})/(\sqrt{\beta}\epsilon)$. At $x = 0$: (a) real component; (b) imaginary component; (c) magnitude. At $x = 1$: (d) real component; (e) imaginary component; (f) magnitude. Results given for $\beta = 10$ (medium dashes), $\beta = 30$ (long dashes), $\beta = 100$ (dot-dashed line), $\beta = 1000$ (dotted line), $\beta = 10000$ (solid line).

We also recover the trivial solution for the leading-order mean velocity:

$$\bar{v}_{H|i}^{(0)} = 0. \quad (4.21)$$

The leading-order temperature distribution satisfies the classical heat diffusion equation, where the solution is antisymmetric in y ,

$$\tau_H^{(0)} = x\epsilon \frac{\sinh(y\delta)}{\sinh\left(\frac{\delta}{2}\right)}, \quad (4.22)$$

with $\delta = \sqrt{-i\beta}$. The leading-order pressure $P_H^{(0)}$ is again gradient-free.

The first-order ($n = 1$) mean normal velocity must satisfy no-penetration at each wall. The slip boundary conditions for the first-order mean tangential velocity are

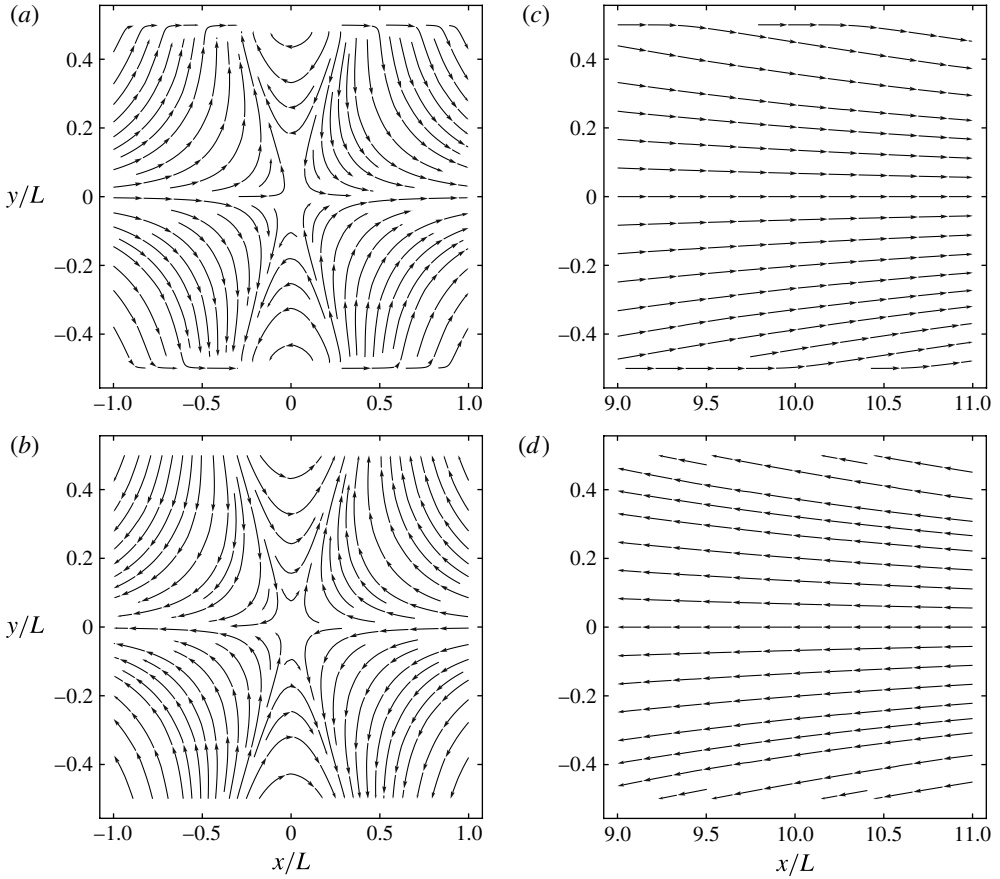


FIGURE 13. Streamlines of symmetric problem for $\beta = 1000$. Flow centred at $x = 0$: (a) real; (b) imaginary. Flow centred at $x = 10$: (c) real; (d) imaginary.

identical to the corresponding steady problem, and take the form (see table 2)

$$\bar{v}_{H|x}^{(1)}|_{y=\pm 1/2} = \mp K_1 \epsilon. \tag{4.23}$$

The unique solution to the first-order equations is

$$P_H^{(1)} = G, \tag{4.24a}$$

$$\tau_H^{(1)} = -x d_1 \epsilon \frac{\sinh(y\delta)}{\tanh\left(\frac{\delta}{2}\right) \sinh\left(\frac{\delta}{2}\right)} + \frac{2}{5} G \left(1 - \frac{\sinh(y\delta)}{\cosh\left(\frac{\delta}{2}\right)} \right) \tag{4.24b}$$

$$\bar{v}_{H|y}^{(1)} = \frac{x\delta\epsilon}{2 \sinh\left(\frac{\delta}{2}\right)} \left[\cosh(y\delta) - \cosh\left(\frac{\delta}{2}\right) \right], \tag{4.24c}$$

$$\bar{v}_{H|x}^{(1)} = \epsilon \left[-K_1 \frac{\sinh(y\delta)}{\sinh\left(\frac{\delta}{2}\right)} + \frac{\delta}{4 \tanh\left(\frac{\delta}{2}\right)} \left(\frac{\sinh(y\delta)}{\sinh\left(\frac{\delta}{2}\right)} - 2y \right) \right], \quad (4.24d)$$

$$P_H^{(2)} = \frac{x\delta^2\epsilon}{2 \sinh\left(\frac{\delta}{2}\right)} \left[\sinh(y\delta) - y\delta \cosh\left(\frac{\delta}{2}\right) \right] + H. \quad (4.24e)$$

Note that, as for the symmetric analysis, closure of the leading-order pressure is achieved at the first-order analysis, and yields $P_H^{(0)} = 0$. The constants G and H in the first- and second-order pressures can also be evaluated at subsequent order, i.e. $n = 2$ and $n = 3$, respectively.

The corresponding Knudsen layer corrections are then obtained by substituting (4.21) and (4.22) into the formulae in table 2, yielding

$$\tau_k^{(1)} = \frac{x\delta\epsilon}{\tanh\left(\frac{\delta}{2}\right)} \left[-\Theta_1 \left(\frac{\frac{1}{2} - y}{k} \right) + \Theta_1 \left(\frac{\frac{1}{2} + y}{k} \right) \right], \quad (4.25a)$$

$$\bar{v}_{K|x}^{(1)} = \frac{1}{2} \left[-Y_1 \left(\frac{\frac{1}{2} - y}{k} \right) + Y_1 \left(\frac{\frac{1}{2} + y}{k} \right) \right], \quad (4.25b)$$

where the functions Θ_1 and Y_1 are defined in (3.8), with associated coefficients c_n given in appendix B.

As noted for the symmetric problem, the spatial dependence of the Knudsen layer corrections in (4.25) is also independent of the oscillation frequency, i.e. independent of β . The forms are thus identical to the corresponding steady flow equations. As such, the following analysis focuses explicitly on the bulk flow results in (4.21), (4.22) and (4.24). Together with (4.25), these give the complete solution to $O(k)$.

4.2.1. Physical analysis of the flow

Plots of the real component, imaginary component, and the magnitude of $\tau_H^{(0)}/(x\epsilon)$ are given in figure 14. As for the symmetric case, a shift in the phase of the gas temperature response is observed as β increases. Boundary layers again form near the walls in the high inertia limit, and the temperature perturbations decay exponentially away from the walls.

The average normal velocity u_y between the walls in the upper half-channel is

$$u_y = 2 \int_0^{1/2} \bar{v}_{H|y}^{(1)} dy = -\frac{x\epsilon}{2} \left(\delta \coth\left(\frac{\delta}{2}\right) - 2 \right), \quad (4.26)$$

with corresponding small- and large- β asymptotics

$$u_y = x\epsilon \begin{cases} \frac{i\beta}{12} - \frac{\beta^2}{720}, & \beta \ll 1, \\ -\frac{-1+i}{2} \sqrt{\frac{\beta}{2}} + 1, & \beta \gg 1. \end{cases} \quad (4.27)$$

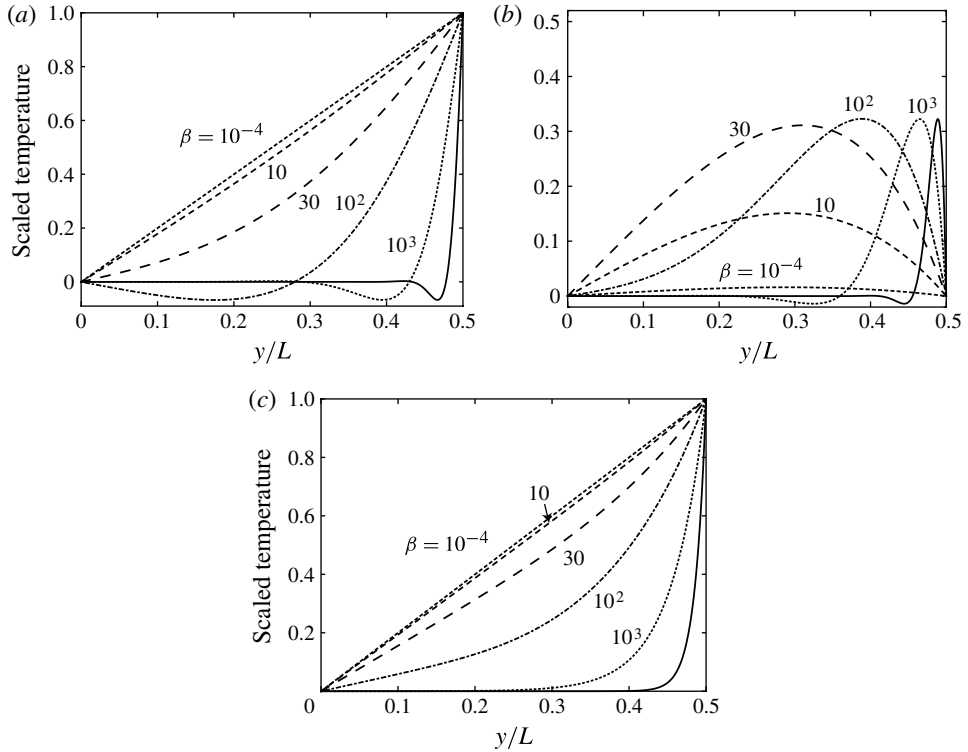


FIGURE 14. Scaled leading-order temperature perturbation of antisymmetric problem $\tau_H^{(0)}/(x\epsilon)$. (a) Real component; (b) imaginary component; (c) magnitude. Results given for $\beta = 1$ (short dashes), $\beta = 10$ (medium dashes), $\beta = 30$ (long dashes), $\beta = 100$ (dot-dashed line), $\beta = 1000$ (dotted line), $\beta = 10\,000$ (solid line).

Analogously, the average tangential velocity u_x is

$$u_x = \frac{\epsilon}{8} \left[-\delta \coth\left(\frac{\delta}{2}\right) + 2 \left(1 - \frac{8K_1 \tanh\left(\frac{\delta}{4}\right)}{\delta} + \tanh^2\left(\frac{\delta}{4}\right) \right) \right], \quad (4.28)$$

with the small- and large- β asymptotic expansions of u_x being

$$u_x = \epsilon \begin{cases} -\frac{K_1}{2} - \frac{i\beta}{192} (2K_1 - 1) + \beta^2 \left(\frac{7}{23\,040} + \frac{K_1}{3840} \right), & \beta \ll 1, \\ \frac{-1 + i}{8} \sqrt{\frac{\beta}{2}} + \frac{1}{2}, & \beta \gg 1. \end{cases} \quad (4.29)$$

The slip coefficient $K_1 = -0.383161\dots < 0$, as before.

As for the symmetric case, the asymptotic formulae in (4.27) and (4.29) accurately describe the behaviour of u_y and u_x in their appropriate limits, and can thus be used to explore the underlying physics of the flow.

Zero inertia ($\beta = 0$). Temperature perturbations at the walls generate an antisymmetric thermal creep in the tangential direction. This corresponds to the first term in the low inertia asymptotic expansion for u_x in (4.29), with corresponding mean

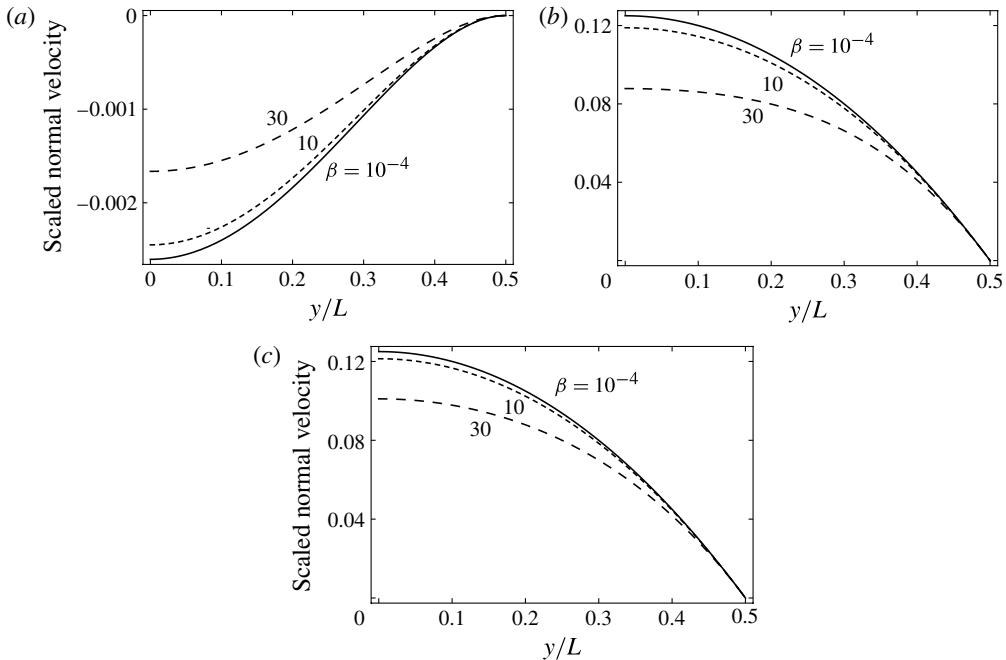


FIGURE 15. Scaled mean normal velocity of antisymmetric problem $\bar{v}_{H|y}^{(1)}/(x\beta^l\epsilon)$, where l is chosen to match dominant asymptotic behaviour in β . Real ($l = 2$), imaginary and magnitude ($l = 1$). (a) Real component; (b) imaginary component; (c) magnitude. Results given for $\beta = 10^{-4}$ (solid line), $\beta = 10$ (medium dashes), $\beta = 30$ (long dashes).

velocity

$$\bar{v}_{H|x,anti}^{(1)} = -2yK_1\epsilon, \quad \bar{v}_{H|y,anti}^{(1)} = 0, \quad (4.30)$$

where the subscript ‘anti’ is used to identify this as the antisymmetric solution for zero inertia.

Small inertia ($\beta \ll 1$). For small inertia, the oscillatory (time-varying) temperature, pressure and density perturbations all contribute to a mean flow in addition to the usual thermal creep (at zero inertia). Near the reference point at $x = 0$, compressibility is again negligible and the mean velocity is divergence-free. Unlike the symmetric problem, however, the average tangential velocity u_x is independent of x due to the antisymmetric wall temperature gradients. Away from the reference point, $x = 0$, gas compressibility becomes significant; this generates a non-zero average normal velocity u_y between the walls, but the average tangential velocity u_x remains unchanged.

The mean normal velocity $\bar{v}_{H|y}^{(1)}$ is presented in figure 15. The solution is proportional to x , and is appropriately scaled for simplicity. This figure clearly illustrates non-penetration at the walls, and the range of validity of the low- β asymptotics for u_y . This solution represents both the unsteady correction and the complete bulk mean normal velocity. This is because the classical thermal creep problem has an identically zero mean normal velocity, from (4.30).

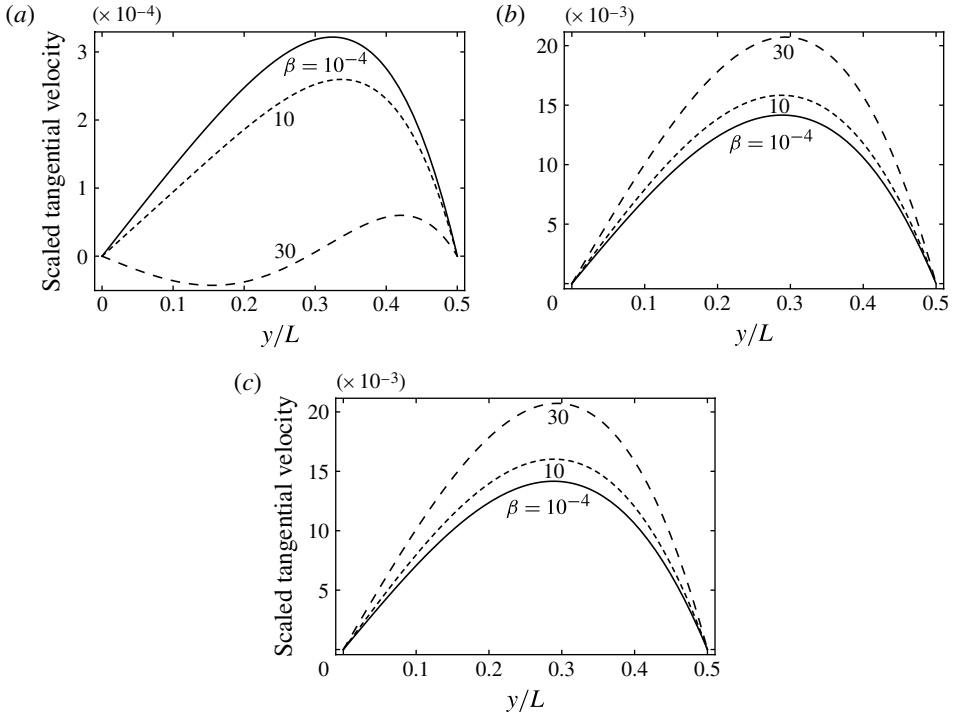


FIGURE 16. Scaled unsteady correction to mean tangential velocity of antisymmetric problem $(\bar{v}_{H|x}^{(1)} - \bar{v}_{H|x,anti}^{(1)})/(\beta^l \epsilon)$, where l is chosen to match dominant asymptotic behaviour in β . Real ($l = 2$); imaginary and magnitude ($l = 1$). (a) Real component; (b) imaginary component; (c) magnitude. Results given for $\beta = 10^{-4}$ (solid line), $\beta = 10$ (medium dashes), $\beta = 30$ (long dashes).

Plots for the unsteady correction to the mean tangential velocity $\bar{v}_{H|x}^{(1)}$ are given in figure 16. We remind the reader that the unsteady correction is defined as the difference between $\bar{v}_{H|x}^{(1)}$ and the classical thermal creep solution from (4.30). As in the symmetric problem, this unsteady correction must satisfy no-slip at the walls; velocity slip in the complete mean tangential velocity drives the steady component of the thermal creep flow. Antisymmetry in temperatures at the walls generates tangential pressure and temperature gradients in the gas that are independent of x . As discussed, the mean tangential flow driven by these gradients is thus also x -independent. For small β , the tangential pressure and temperature gradients are given by

$$\left. \begin{aligned} \frac{\partial \tau_H^{(0)}}{\partial x} &= 2y\epsilon - \frac{i\beta\epsilon}{12} (4y^3 - y), \\ \frac{\partial P_H^{(2)}}{\partial x} &= \beta^2\epsilon \left(\frac{y^3}{6} - \frac{y}{6} \right) - \frac{i\beta^3\epsilon}{5760} (48y^5 - 40y^3 + 15y), \end{aligned} \right\} \beta \ll 1, \quad (4.31)$$

which are both antisymmetric in y . In the limit of small β , effects due to the tangential temperature gradient in the gas dominate those from the tangential pressure gradient. This temperature gradient, together with the no-slip condition on the unsteady correction, leads to the flow profiles in figure 16 for $\beta = 10^{-4}$. Streamlines of the complete bulk flow at $\beta = 10^{-4}$ are given in figure 17. A critical point at the origin is

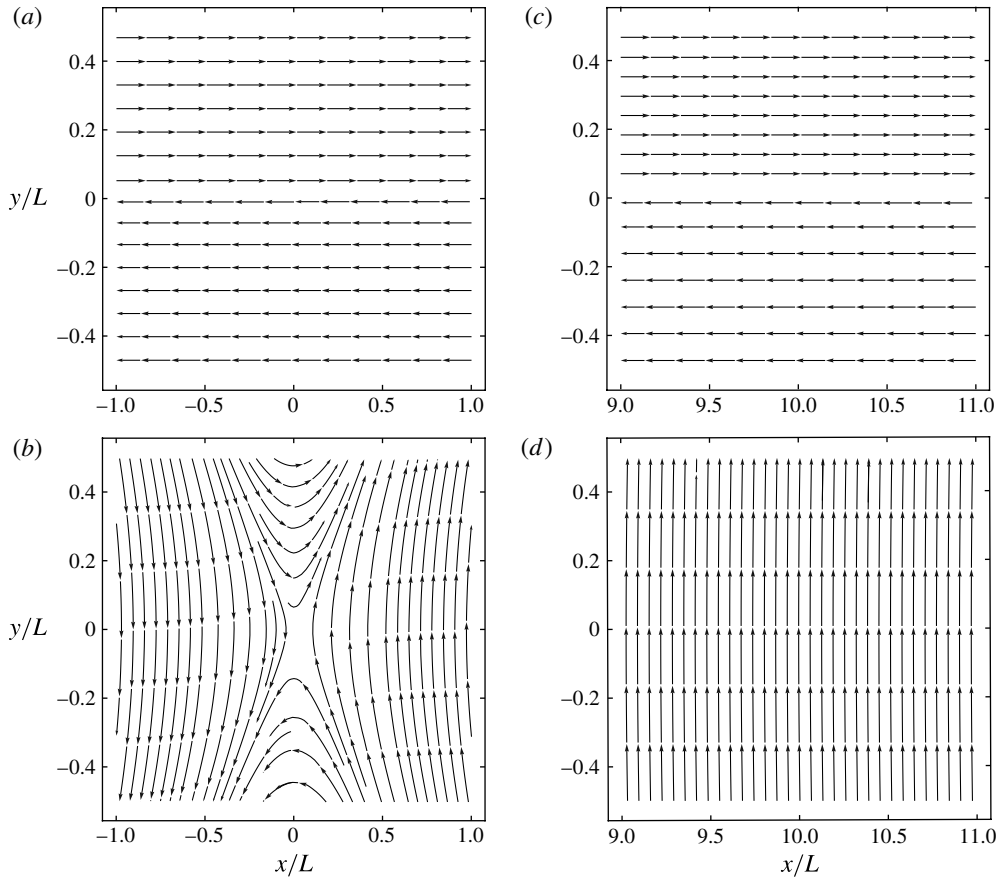


FIGURE 17. Streamlines of antisymmetric problem for $\beta = 10^{-4}$. Flow centred at $x = 0$: (a) real; (b) imaginary. Flow centred at $x = 10$: (c) real; (d) imaginary.

present in the real component (figure 17a), due to reversal of the velocity field across the line $y = 0$. A critical point (saddle node) at the origin also clearly exists in the imaginary component; see figure 17(b).

Intermediate inertia ($\beta \sim 1$). As inertia increases, the tangential pressure gradient in the gas increases; see (4.31). For $\beta = 10$, no significant change in the unsteady correction profile is observed in figure 16. However, for $\beta = 30$, a significant pressure gradient is present and leads directly to inflection in the real component of the unsteady correction to the mean tangential velocity, as illustrated in figure 16(a). No new critical points arise, despite the unsteady correction being zero away from the origin: this is because the classical thermal creep solution in (4.30) is only zero at the origin. No inflection is observed in the imaginary component, since the low- β asymptotic in the pressure gradient is dominated by its real component; see (4.31) and figure 16(b).

Streamlines for the complete bulk flow at $\beta = 30$ are given in figure 18; once more, plots about the reference point $x = 0$, and $x = 10$, are included. The critical point mentioned in the real component of the velocity for small β is now clearly identified as a centre; see figure 18(a). This contrasts with the imaginary component

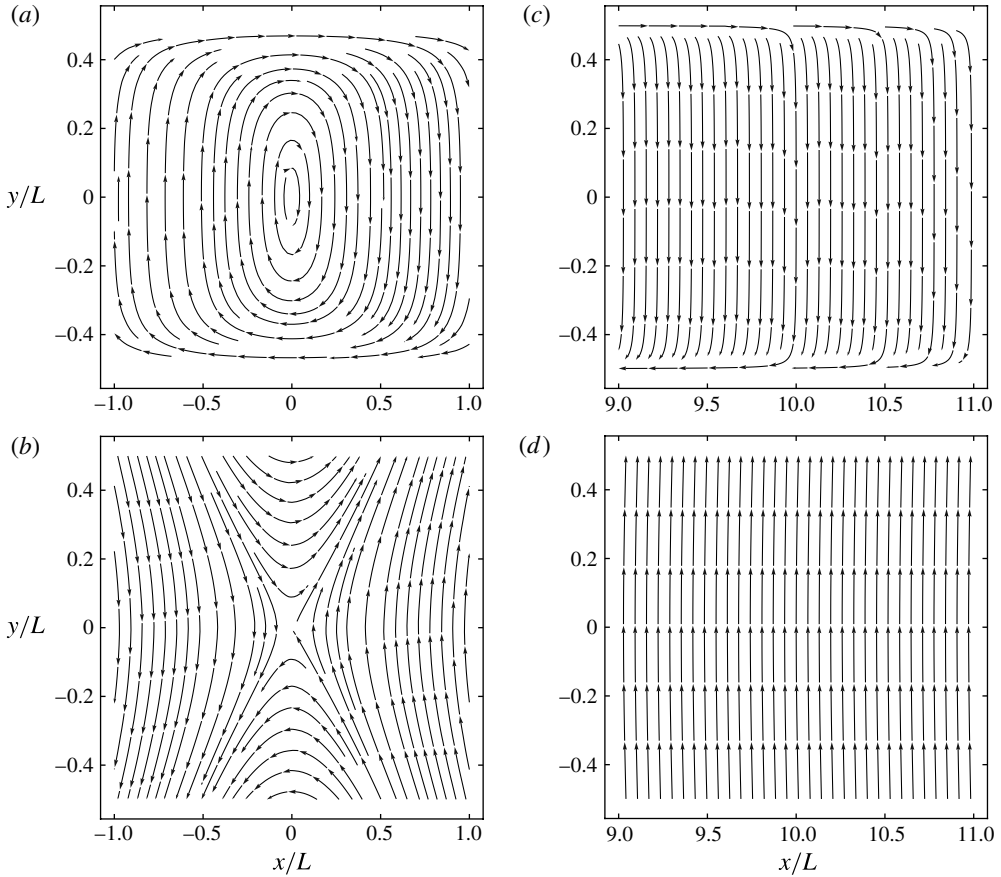


FIGURE 18. Streamlines of antisymmetric problem for $\beta = 30$. Flow centred at $x = 0$: (a) real; (b) imaginary. Flow centred at $x = 10$: (c) real; (d) imaginary.

in figure 18(b), where the critical saddle point observed for small β persists. As we move away from the origin, the magnitude of the mean tangential velocity remains unchanged because it is independent of x . However, the mean normal velocity increases considerably in magnitude due to gas compressibility, resulting in a set of almost vertical streamlines for large x : for example, see results for $x = 10$ in figure 18(c–d).

High inertia ($\beta \gg 1$). Similar behaviour to the symmetric problem is observed in the high inertia limit. Temperature perturbations are confined to the walls; see figure 14. Pressure gradients within the thermal boundary layers are large, and these gradients drive similarly large gradients in the mean velocity; see figures 19 and 20.

Flow is incompressible outside the boundary layers. However, the mean tangential velocity $\bar{v}_{H|x}^{(1)}$ is independent of x everywhere, due to the antisymmetric boundary temperature gradients; see (4.24). Since the flow is divergence-free outside the boundary layers, it then immediately follows that the normal velocity outside the thermal boundary layers is independent of y . This is clearly illustrated in figure 19.

Outside the boundary layers, a linear variation in the unsteady correction to the mean tangential velocity $\bar{v}_{H|x}^{(1)}$ is, however, evident. This is consistent with the large- β

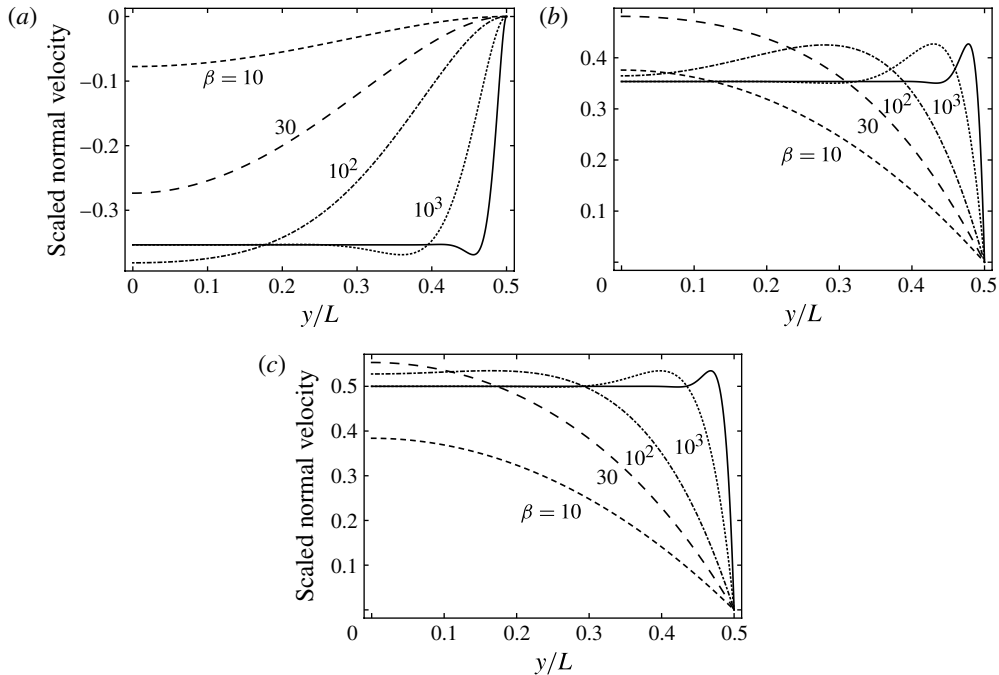


FIGURE 19. Scaled mean normal velocity of antisymmetric problem $\bar{v}_{Hy}^{(1)}/(x\sqrt{\beta}\epsilon)$. (a) Real component; (b) imaginary component; (c) magnitude. Results given for $\beta = 10$ (medium dashes), $\beta = 30$ (long dashes), $\beta = 100$ (dot-dashed line), $\beta = 1000$ (dotted line), $\beta = 10000$ (solid line).

asymptotic result for the pressure $P_H^{(2)}$,

$$\frac{\partial P_H^{(2)}}{\partial x} = -\frac{y\beta^{3/2}\epsilon}{2\sqrt{2}}(1+i), \quad \beta \gg 1, \quad (4.32)$$

which is proportional to y . The mean tangential flow outside the boundary layers is thus driven by tangential pressure gradients in the gas. This is identical to the conclusion drawn for the symmetric problem.

To elucidate the structure of the flow at high β , streamlines for the complete bulk flow at $\beta = 1000$ about the reference point $x = 0$ are given in figure 21. Previously, we observed two critical points at the origin $(x, y) = (0, 0)$ for intermediate inertia: a centre in the real component, and a saddle in the imaginary; see figure 18(a,b). As β increases, the centre in the real component (figure 18a) bifurcates to yield two centres along the line $x = 0$. The original centre directly at the origin thus becomes a saddle point, as illustrated in figure 21(a) for $\beta = 1000$. This bifurcation occurs when the unsteady parameter β equals the critical value

$$\beta_c = 35.2392 \dots \quad (4.33)$$

As β increases above this critical value, the two centres then migrate towards the walls, and at high β lie within the thermal boundary layers. These centres are illustrated in figure 22 for $\beta = 1000$, and occur at $x = 0$ and $y = \pm 0.486368L$. Physically, these critical points arise due to a balance between the pressure gradient and velocity slip at the walls.

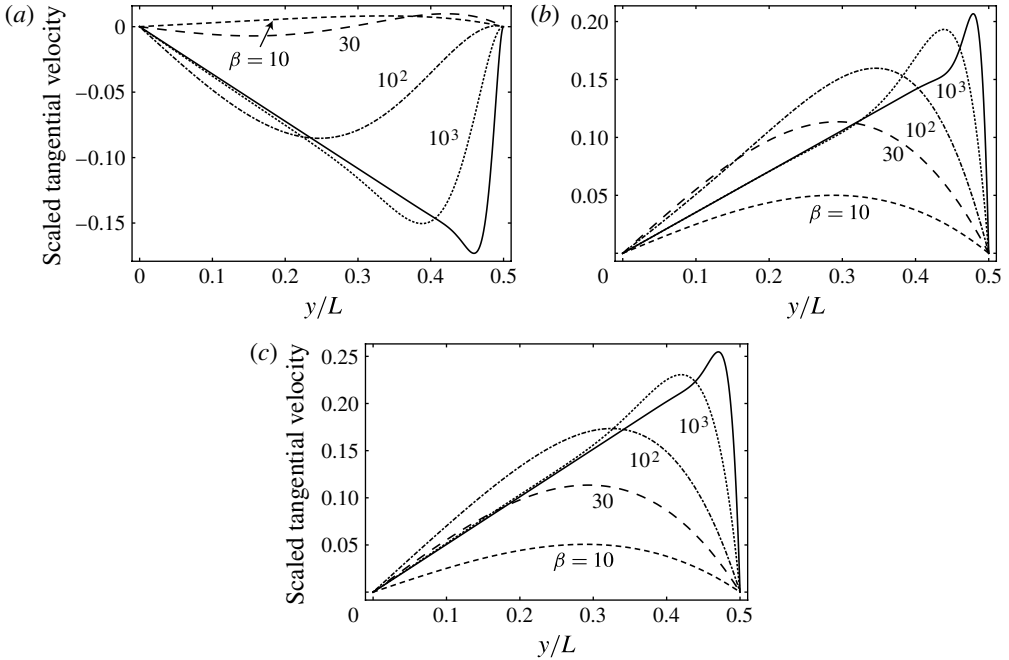


FIGURE 20. Scaled unsteady correction to mean tangential velocity of antisymmetric problem $(\bar{v}_{H|x}^{(1)} - \bar{v}_{H|x,anti}^{(1)})/(\sqrt{\beta}\epsilon)$. (a) Real component; (b) imaginary component; (c) magnitude. Results given for $\beta = 10$ (medium dashes), $\beta = 30$ (long dashes), $\beta = 100$ (dot-dashed line), $\beta = 1000$ (dotted line), $\beta = 10000$ (solid line).

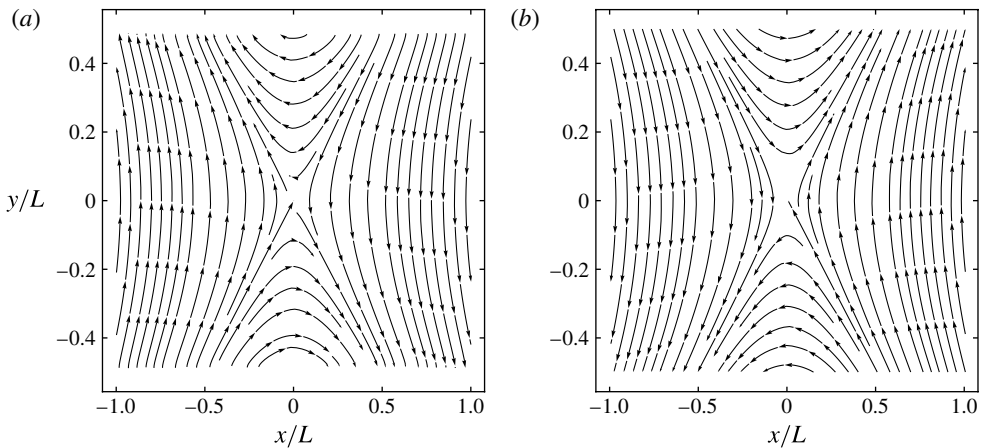


FIGURE 21. Streamlines of antisymmetric problem for $\beta = 1000$. Flow centred at $x = 0$: (a) real; (b) imaginary.

Away from $x = 0$, the streamlines are similar to those obtained for the $\beta = 30$ case in figure 18(c-d), and are hence omitted for brevity.

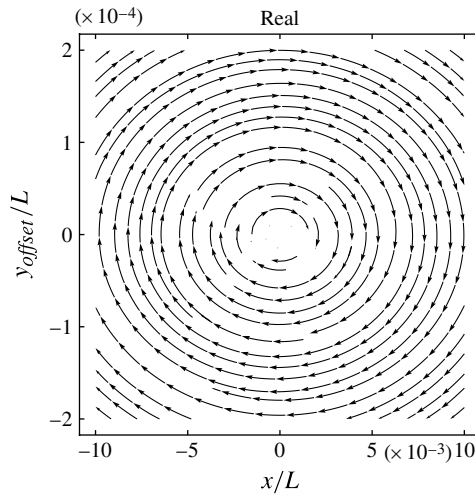


FIGURE 22. Streamlines of antisymmetric problem for $\beta = 1000$, with the upper boundary layer. Flow centred at the critical point in the upper half-plane, $(x, y) = (0, 0.486368L)$. Zoomed image of figure 21(a) for $-0.01 \leq x/L \leq 0.01$ and $-0.0002 \leq y_{\text{offset}}/L \leq 0.0002$, where $y_{\text{offset}} = y - 0.486368L$.

5. Conclusions

We have theoretically investigated the effect of oscillatory (time-varying) boundary conditions and body forces on slightly rarefied gas flows. This generalizes the theory proposed by Sone for steady and slightly rarefied flows over solid walls using the BGK kinetic model (Sone 1969, 1974). Modern rarefied flows are distinctly oscillatory and unsteady, and this article has addressed the effect of this motion on the governing equations, slip models and Knudsen layer corrections. To second order in the Knudsen number, we have shown that the well-known second-order tangential velocity slip model and Knudsen layer correction remain unaltered by oscillatory motion. This finding validates application of the conventional steady second-order slip boundary condition to the analysis of oscillatory flows. This contrasts with all other second-order slip components and Knudsen layer corrections, which are modified by unsteady motion.

Application of this general theory was illustrated for oscillatory thermal creep between two infinite and parallel walls. The leading-order effect of oscillatory motion, for small Knudsen number, was calculated for two canonical problems: (i) where the temperature gradients at the walls are symmetric; and (ii) where they are antisymmetric. Linear superposition of these results directly gives the solution for arbitrary symmetry between the walls. Time-varying temperature gradients were found to not alter the classical (steady) thermal creep, but induce an additional (out-of-phase) flow which is driven by perturbations to the gas temperature $\tau_H^{(0)}$, pressure $P_H^{(2)}$, and density $\sigma_H^{(0)}$. For low inertia, incompressible bulk flow exists near the reference point of zero temperature oscillations ($x = 0$), with gas compressibility dominating away from this point. This contrasts with the high inertia limit where flow outside the thermal boundary layers is incompressible throughout the channel. Qualitatively different behaviours were observed for symmetric and antisymmetric wall temperature

$$\begin{aligned}
 \sqrt{\pi}\bar{v}_{K|i}^{(2)}t_i^1 &= \mathcal{L}_0 \left(\bar{v}_{K|i}^{(2)}t_i^1(\eta) \right) - \left(\bar{v}_{H|i}^{(2)} - V_i^{(2)} \right) t_i^1 J_0 - S_{H|ij}^{(1)} n_i t_j^1 J_1 + \frac{1}{2} \frac{\partial \tau_b^{(1)}}{\partial x_i} t_i^1 \left(J_2 - \frac{1}{2} J_0 \right) \\
 &+ n_j \frac{\partial S_{H|ik}^{(0)}}{\partial x_j} n_k t_i^1 \left(J_2 - \frac{1}{2} J_0 \right) + \frac{\partial G_{H|i}^{(0)}}{\partial x_j} t_j^1 n_i \left(\frac{C_1}{2} J_0 \right) \\
 &+ \kappa_{ij} t_j^1 S_{H|ik}^{(0)} n_k \left(k_0 J_1 + J_2 - \frac{1}{2} J_0 \right) - \bar{\kappa} S_{H|ij}^{(0)} n_i t_j^1 \left(\sqrt{\pi} \int_{-\infty}^{\eta} Y_0(\eta_0) d\eta_0 + J_0 \right) \\
 &+ \kappa_{ij} t_j^1 G_{H|j}^{(0)} \left(\frac{C_1}{2} J_0 - \frac{1}{2} J_3 + \left(K_1 + \frac{1}{4} \right) J_1 \right) - \bar{\kappa} G_{H|i}^{(0)} t_i^1 \left(J_3 + \frac{\sqrt{\pi}}{2} \int_{-\infty}^{\eta} Y_1(\eta_0) d\eta_0 \right) \\
 \\
 \sqrt{\pi}\bar{v}_{K|i}^{(2)}n_i &= \int_0^{\infty} \left[\sigma_K^{(2)} J_0 (|\eta - \eta_0|) + \tau_K^{(2)} \left(J_2 (|\eta - \eta_0|) - \frac{1}{2} J_0 (|\eta - \eta_0|) \right) \right] \text{sgn}(\eta - \eta_0) d\eta_0 \\
 &+ 2 \int_0^{\infty} \bar{v}_{K|i}^{(2)} n_i J_1 (|\eta - \eta_0|) d\eta_0 - \left(\sigma_H^{(2)} - \sigma_b^{(2)} \right) J_1 - 2 \left(\bar{v}_{H|i}^{(2)} - V_i^{(2)} \right) n_i J_2 \\
 &- \left(\tau_H^{(2)} - \tau_b^{(2)} \right) \left(J_3 - \frac{1}{2} J_1 \right) - G_{H|i}^{(1)} n_i \left(J_4 - \frac{3}{2} J_2 \right) + \frac{4}{3} \frac{\partial \bar{v}_{H|i}^{(1)}}{\partial x_i} \left(J_3 - \frac{1}{2} J_1 \right) \\
 &+ \frac{\partial S_{H|ij}^{(0)}}{\partial x_k} n_i n_j n_k \left[\frac{k_0}{2} J_1 + \frac{1}{2} \mathcal{L}_3 [Y_0(\eta)] \right] + \frac{\partial G_{H|ij}^{(0)}}{\partial x_j} n_i n_j \left[K_1 J_1 + \frac{1}{2} J_3 - \frac{1}{4} J_1 \right. \\
 &\left. + \frac{1}{2} \mathcal{L}_3 [Y_1(\eta)] \right] + \frac{\partial G_{H|i}^{(0)}}{\partial x_i} \left[-K_1 J_1 + J_5 - \frac{17}{6} J_3 + \frac{2}{3} J_1 - \frac{1}{2} \mathcal{L}_3 [Y_1(\eta)] \right] \\
 &+ 2\bar{\kappa} G_{H|i}^{(0)} n_i \left[K_1 J_1 - C_1 \left(J_4 - \frac{3}{2} J_2 \right) - d_1 \left(J_6 - 4J_4 + \frac{9}{4} J_2 \right) + J_7 - 5J_5 \right. \\
 &\left. + \frac{17}{4} J_3 - \frac{1}{4} J_1 + \frac{1}{2} \mathcal{L}_3 [Y_1(\eta)] + \int_0^{\infty} \left(\Omega_1 \left(J_3 (|\eta - \eta_0|) - \frac{3}{2} J_1 (|\eta - \eta_0|) \right) \right. \right. \\
 &\left. \left. + \Theta_1 \left(J_5 (|\eta - \eta_0|) - 3J_3 (|\eta - \eta_0|) + \frac{3}{4} J_1 (|\eta - \eta_0|) \right) \right) d\eta_0 \right] + \left(\kappa_{ij} \kappa_{ji} V_k^{(0)} n_k \right. \\
 &\left. + \left(t_k^1 \frac{\partial}{\partial x_k} + g_2 \right) \left[t_j^1 \frac{\partial \left(V_i^{(0)} n_i \right)}{\partial x_j} \right] + \left(t_k^2 \frac{\partial}{\partial x_k} - g_1 \right) \left[t_j^2 \frac{\partial \left(V_i^{(0)} n_i \right)}{\partial x_j} \right] \right) [k_0 J_1 \\
 &- 2J_4 + 3J_2 + 2 \int_0^{\infty} Y_0(\eta_0) \left[J_2 (|\eta - \eta_0|) - \frac{1}{2} J_0 (|\eta - \eta_0|) \right] \text{sgn}(\eta - \eta_0) d\eta_0]
 \end{aligned}$$

TABLE 4. Second-order Knudsen layer governing equations for the mean tangential velocity, $\sqrt{\pi}\bar{v}_{K|i}^{(2)}t_i^1$, and mean normal velocity, $\sqrt{\pi}\bar{v}_{K|i}^{(2)}n_i$.

distributions in these two inertial limits, and the physical mechanisms driving these flows were explored.

Acknowledgements

The authors acknowledge financial support from an Australian Postgraduate Award and the Australian Research Council Grants Scheme.

$$\begin{aligned}
 \sqrt{\pi}\sigma_K^{(2)} &= \mathcal{L}_1 \left[\sigma_K^{(2)}(\eta), \tau_K^{(2)}(\eta) \right] + 2J_0(\eta)\mathcal{E}_1 \left[\sigma_K^{(2)}(\eta), \tau_K^{(2)}(\eta) \right] \\
 &\quad - \left(\tau_H^{(2)} - \tau_b^{(2)} \right) [J_2 - J_0] + \frac{4}{3} \frac{\partial \bar{v}_{Hi}^{(1)}}{\partial x_i} [J_2 - J_0] - G_{Hi}^{(1)} n_i \left[J_3 - \frac{3}{2} J_1 \right] \\
 &\quad + \frac{\partial S_{Hij}^{(0)}}{\partial x_k} n_i n_j n_k \left[\frac{\sqrt{\pi}}{4} J_0 - \frac{1}{2} J_1 \right] + \frac{\partial G_{Hi}^{(0)}}{\partial x_i} \left[J_4 - \frac{7}{3} J_2 + \frac{1}{3} J_0 \right] \\
 &\quad + 2\bar{\kappa} G_{Hi}^{(0)} n_i \left[-2J_0 \mathcal{E}_7 [\Omega_1(\eta), \Theta_1(\eta)] + \frac{1}{4} J_0 + d_1 (J_3 + J_1) - 2J_4 \right. \\
 &\quad \left. + \frac{1}{2} J_2 - \int_0^\infty \Theta_1 (J_2 + J_0) \operatorname{sgn}(\eta - \eta_0) d\eta_0 \right] \\
 &\quad + \left(\kappa_{ij} \kappa_{ji} V_k^{(0)} n_k + \left(t_k^1 \frac{\partial}{\partial x_k} + g_2 \right) \left[t_j^1 \frac{\partial (V_i^{(0)} n_i)}{\partial x_j} \right] \right. \\
 &\quad \left. + \left(t_k^2 \frac{\partial}{\partial x_k} - g_1 \right) \left[t_j^2 \frac{\partial (V_i^{(0)} n_i)}{\partial x_j} \right] \right) \left[-2J_3 + 2J_1 + \frac{\sqrt{\pi}}{2} J_0 \right] \\
 \\
 \frac{3}{2} \sqrt{\pi} \tau_K^{(2)} &= \mathcal{L}_2 \left[\sigma_K^{(2)}(\eta), \tau_K^{(2)}(\eta) \right] + 2 \left[J_2(\eta) - \frac{1}{2} J_0(\eta) \right] \mathcal{E}_1 \left[\sigma_K^{(2)}(\eta), \tau_K^{(2)}(\eta) \right] \\
 &\quad - \left(\tau_H^{(2)} - \tau_b^{(2)} \right) \left[J_4 - \frac{3}{2} J_2 + \frac{3}{2} J_0 \right] + \frac{\partial \bar{v}_{Hi}^{(1)}}{\partial x_i} \left[\frac{4}{3} J_4 - 2J_2 - \frac{5}{6} J_0 \right] \\
 &\quad - G_{Hi}^{(1)} n_i \left[J_5 - 2J_3 + \frac{7}{4} J_1 \right] \\
 &\quad + \frac{\partial S_{Hij}^{(0)}}{\partial x_k} n_i n_j n_k \left[\frac{\sqrt{\pi}}{4} \left(J_2 - \frac{1}{2} J_0 \right) - \frac{1}{2} J_3 + \frac{1}{4} J_1 \right] \\
 &\quad + \frac{\partial G_{Hi}^{(0)}}{\partial x_i} \left[J_6 - \frac{17}{4} J_4 + \frac{15}{6} J_2 - J_0 \right] \\
 &\quad + \bar{\kappa} G_{Hi}^{(0)} n_i \left[4J_3 \mathcal{E}_1 [\Omega_1(\eta), \Theta_1(\eta)] - 4 \left(J_2 - \frac{1}{2} J_0 \right) \mathcal{E}_7 [\Omega_1(\eta), \Theta_1(\eta)] \right. \\
 &\quad \left. + d_1 J_3 - 2J_6 + 2J_4 - 3J_2 - \frac{1}{4} J_0 + 2 \int_0^\infty \Omega_1 J_2 (|\eta - \eta_0|) \operatorname{sgn}(\eta - \eta_0) d\eta_0 \right. \\
 &\quad \left. - \sqrt{\pi} \int_\infty^\eta \Omega_1 d\eta_0 + \frac{3\sqrt{\pi}}{2} \int_\infty^\eta \Theta_1 d\eta_0 \right] \\
 &\quad + \left(\kappa_{ij} \kappa_{ji} V_k^{(0)} n_k + \left(t_k^1 \frac{\partial}{\partial x_k} + g_2 \right) \left[t_j^1 \frac{\partial (V_i^{(0)} n_i)}{\partial x_j} \right] \right. \\
 &\quad \left. + \left(t_k^2 \frac{\partial}{\partial x_k} - g_1 \right) \left[t_j^2 \frac{\partial (V_i^{(0)} n_i)}{\partial x_j} \right] \right) \left[-2J_5 + 3J_3 + \frac{\sqrt{\pi}}{2} \left(J_2 - \frac{1}{2} J_0 \right) \right]
 \end{aligned}$$

TABLE 5. Second-order Knudsen layer governing equations for the density perturbation, $\sqrt{\pi}\sigma_K^{(2)}$, and temperature perturbation, $(3/2)\sqrt{\pi}\tau_K^{(2)}$.

Appendix A. Second-order Knudsen layer equations and ancillary relations

In this appendix, we list the set of second-order Knudsen layer governing equations; see tables 4 and 5. All bulk flow quantities are evaluated at the wall. Abramowitz functions (see (3.9)) that are presented with no argument, J_n , implicitly take an argument of η , i.e. $J_n(\eta)$. We have made use of the definitions and formulae in tables 6 and 7 in defining the equations in tables 4 and 5.

Appendix B. Slip and Knudsen layer function coefficients

The solutions to the Knudsen layer equations in tables 4 and 5 are given in table 3. Tables 8–11 summarize the associated slip coefficients and Knudsen layer function coefficients c_n that appear in these solutions. The complete set of bulk flow slip coefficients are given in table 8. The Knudsen layer correction coefficients c_n are given in tables 9–11. The Knudsen layer correction coefficients c_n are provided to ensure at least 4 significant figure accuracy in the resulting functions; omitted coefficients are not required for this level of accuracy.

The coefficients of the function Y_{a1} are omitted in the presentation, since

$$Y_{a1}(\eta) = -Y_1(\eta). \tag{B 1}$$

$$\begin{aligned} \mathcal{L}_0[f(\eta)] &= \int_0^\infty f(\eta_0) J_{-1}(|\eta - \eta_0|) \, d\eta_0, \\ \mathcal{L}_3[f(\eta)] &= \int_0^\infty f(\eta_0) [2J_2(|\eta - \eta_0|) - J_0(|\eta - \eta_0|)] \operatorname{sgn}(\eta - \eta_0) \, d\eta_0, \\ \mathcal{L}_1[f(\eta), w(\eta)] &= \int_0^\infty \left[f(\eta_0) J_{-1}(|\eta - \eta_0|) + w(\eta_0) \left(J_1(|\eta - \eta_0|) - \frac{1}{2} J_{-1}(|\eta - \eta_0|) \right) \right] \, d\eta_0, \\ \mathcal{L}_2[f(\eta), w(\eta)] &= \int_0^\infty \left[f(\eta_0) \left(J_1(|\eta - \eta_0|) - \frac{1}{2} J_{-1}(|\eta - \eta_0|) \right) + w(\eta_0) \left(J_3(|\eta - \eta_0|) - J_1(|\eta - \eta_0|) + \frac{5}{4} J_{-1}(|\eta - \eta_0|) \right) \right] \, d\eta_0, \\ \mathcal{E}_1[f(\eta), w(\eta)] &= \int_0^\infty \left[f(\eta_0) J_0(\eta_0) + w(\eta_0) \left(J_2(\eta_0) - \frac{1}{2} J_0(\eta_0) \right) \right] \, d\eta_0, \\ \mathcal{E}_7[f(\eta), w(\eta)] &= \int_0^\infty \left[f(\eta_0) \left(J_3(\eta_0) - \frac{3}{2} J_1(\eta_0) \right) + w(\eta_0) \left(J_5(\eta_0) - 3J_3(\eta_0) + \frac{3}{4} J_1(\eta_0) \right) \right] \, d\eta_0. \end{aligned}$$

TABLE 6. Definitions used in the Knudsen layer analysis.

$$\begin{aligned}
 C_1 &= \frac{d_1}{2} - 2\mathcal{E}_1 [\Omega_1(\eta), \Theta_1(\eta)], \\
 \frac{\partial S_{Hij}^{(0)}}{\partial x_k} n_i n_j t_k^a &= -2\kappa_{ij} S_{Hijk}^{(0)} n_k t_i^a, \\
 S_{Hij}^{(0)} t_i^a t_j^b &= 0, \\
 S_{Hij}^{(0)} n_i n_j &= 0, \\
 \frac{\partial S_{Hij}^{(0)}}{\partial x_j} n_i &= \frac{1}{2} \frac{\partial S_{Hij}^{(0)}}{\partial x_k} n_i n_j n_k - \left(\kappa_{ij} \kappa_{ji} V_k^{(0)} n_k + \left(t_k^1 \frac{\partial}{\partial x_k} + g_2 \right) \left[t_j^1 \frac{\partial (V_i^{(0)} n_i)}{\partial x_j} \right] \right. \\
 &\quad \left. + \left(t_k^2 \frac{\partial}{\partial x_k} - g_1 \right) \left[t_j^2 \frac{\partial (V_i^{(0)} n_i)}{\partial x_j} \right] \right), \\
 S_{Hij}^{(1)} n_i n_j &= -k_0 \frac{\partial S_{Hij}^{(0)}}{\partial x_k} n_i n_j n_k - 2K_1 \left(\frac{\partial G_{Hij}^{(0)}}{\partial x_j} n_i n_j + 2\bar{\kappa} G_{Hij}^{(0)} n_i - \frac{\partial G_{Hij}^{(0)}}{\partial x_i} \right) \\
 &\quad - 2 \frac{\partial \bar{v}_{Hij}^{(1)}}{\partial x_i} - 2k_0 \left(\kappa_{ij} \kappa_{ji} V_k^{(0)} n_k + \left(t_k^1 \frac{\partial}{\partial x_k} + g_2 \right) \left[t_j^1 \frac{\partial (V_i^{(0)} n_i)}{\partial x_j} \right] \right. \\
 &\quad \left. + \left(t_k^2 \frac{\partial}{\partial x_k} - g_1 \right) \left[t_j^2 \frac{\partial (V_i^{(0)} n_i)}{\partial x_j} \right] \right).
 \end{aligned}$$

TABLE 7. Useful formulae for the Knudsen layer analysis. The superscripts *a* and *b* take the values 1, 2.

Coefficient	Value
k_0	-1.0161913030643512
K_1	-0.3831612186208458
a_1	0.7663223775399685
a_2	0.5000011658656275
a_3	-0.2663209722255849
a_4	0.27921841900479466
a_5	0.26692722726049706
a_6	-0.766438720268546
b_1	0.11683882258660261
b_2	0.26692698991326624
d_1	1.3027154398248846
d_4	0.1116873776627049
d_5	1.821808451903212
d_8	2.2765385604509154
d_9	-1.427325823117843
d_{10}	-0.06842936408468211

TABLE 8. Knudsen layer slip coefficients.

c_n	$Y_0(\eta)$	$Y_1(\eta)$	$Y_{a2}(\eta)$	$Y_{a3}(\eta)$	$Y_{a5}(\eta)$	$Y_{a6}(\eta)$
c_0	0.39894279790867226	0.4054020423001202	-0.4053999236980921	-3.2595961423758916 × 10 ⁻⁷	7.057449122121073 × 10 ⁻⁷	0.3057188467476478
c_1	-1.166375116415697	-0.8408819398473782	1.2903433001877047	-0.3674114108928	0.372056182404815	-0.6922245438978492
c_2	5.341195755284069	5.587855242711406	-7.009325517286814	0.48796996519941765	-4.175653843130568	3.8011222044152215
c_3	-15.962300417409859	-20.86322764780027	18.59757071728461	-0.60134305125908	26.229918772809857	-11.187727439346745
c_4	29.389888237590096	48.449653678922665	-24.703458278617262	0.18412646603221156	-75.57301538108658	21.133049836544583
c_5	-32.826456815183604	-68.878484918171759	15.362545825002611	-0.11986696521647763	115.18093510565453	-24.528673945201223
c_6	22.781517506486804	62.32666163972596	-4.236702739531998	0.17201712339064626	-97.78778702865101	18.36842395816561
c_7	-9.823820631658442	-36.24826746523693	0.5162992745362628	-0.1201820220219937	45.911149660154671	-8.811010620804234
c_8	2.5604963888390255	13.427779631926873	-0.12241841014820497	0.01834052957636372	-10.894566393215541	2.621362947010814
c_9	-0.3676243930859195	-3.0296338267092304			0.9543338191200805	-0.42551809560791687
c_{10}	0.022197983174673436	0.376882980415660925			6.051491020858039 × 10 ⁻¹⁰	0.02835425544530687
c_{11}		-0.01973397240652468				

TABLE 9. Coefficients of $Y_m(\eta)$, the Knudsen layer mean tangential velocity functions.

c_n	$\Omega_1(\eta)$	$\Omega_4(\eta)$	$\Omega_5(\eta)$	$\Omega_8(\eta)$	$\Omega_9(\eta)$	$\Omega_{10}(\eta)$
c_0	0.4645150417159274	-0.1576165696461047	0.42909113099699037	0.2700428833281805	-0.42943320833491786	0.6581371128805783
c_1	-1.8785788489664434	0.4991412113656849	-1.6066491852492677	17.235435852351678	-1.2714409973609506	-0.9743478519413286
c_2	9.830594944287945	-2.283147968562475	25.860715972247462	-327.808301599315	8.48828069102768	5.945424939945626
c_3	-32.68210146761804	6.942074382469397	-215.6831593328557	1975.0608631398632	5.75242674419129	-18.56121114817641
c_4	65.12912838051923	-12.844157126647787	956.6949328494577	-5700.4607464663195	-65.49774396335084	35.8276265544993
c_5	-78.93106732673846	14.399483341228299	-2436.979060954567	9190.754120324877	103.35153587279535	-42.355679674848886
c_6	60.41934603739543	-9.974086199256982	3796.3989037507563	-8928.914430858596	-80.61190936342379	31.964390225113572
c_7	-30.064837758684902	4.273229941526988	-3753.237521981633	5409.666274927965	40.3839158886542	-15.50834611029216
c_8	9.946300973193898	-1.096601825461954	2389.1655448970937	-2049.7648364506203	-14.222972077934873	4.6426851954527395
c_9	-2.186586739485301	0.1539259335495705	-970.2345483136455	470.31882474672096	3.1349768119058736	-0.7754521343591912
c_{10}	0.2976361644584244	-0.009084781176822819	241.1051555280483	-59.54564218062861	-0.3138540746291158	0.053655662196282636
c_{11}	-0.018294867611415702		-33.065827725840656	3.183267111214084		
c_{12}			1.884251462696426			

TABLE 10. Coefficients of $\Omega_m(\eta)$, the Knudsen layer density functions.

c_n	$\Theta_1(n)$	$\Theta_4(n)$	$\Theta_5(n)$	$\Theta_8(n)$	$\Theta_9(n)$	$\Theta_{10}(n)$
c_0	-0.47586821852973676	0.014025700359675925	-0.6042546114620624	-0.46742647386036257	0.604418301776068	0.2164485002386916
c_1	1.4854013687672925	-0.16293309113476062	1.3404078119672074	-222.76617971919225	-2.3982657644017293	-0.03403186337521388
c_2	-7.184460010978979	0.8536111697086781	-22.23509110378271	3337.691900988897	21.607346813128885	0.15410227973946392
c_3	21.3542382648883	-2.7330978588646553	188.66076847027122	-17757.895624800247	-68.90904033853698	0.09659722742887016
c_4	-37.446994621552044	5.03724074754132	-860.3902860836627	46887.4564661285	90.67835875531874	0.024917148502478476
c_5	37.84676994179323	-5.564626969165013	2239.190804266879	-70608.39881225425	-43.841961949408386	0.6417935090500556
c_6	-22.178456675332115	3.7601301155701163	-3547.7022387767447	64956.970498024886	-3.659307840655997	-1.6949457839491806
c_7	7.33274798660993	-1.5586231794452052	3556.187873770925	-37631.878236563345	9.148211349476913	1.870674027611385
c_8	-1.3823926607927444	0.3844381129280014	-2291.1420037084577	13737.026481976018	-1.6946054504569499	-0.975960002878931
c_9	0.22081054995310287	-0.05171651551155978	940.75127790173	-3054.8795256342137	-0.339614309343722	0.24191659145176123
c_{10}	-0.048887967057644005	0.0029452295282730123	-236.21800654861087	376.7544709794641	0.10375048765149288	-0.021495328089195378
c_{11}	0.005067301004991428		32.713400685104965	-19.6980817117839667		
c_{12}			-1.880277410787573			

TABLE 11. Coefficients of $\Theta_m(n)$, the Knudsen layer temperature functions.

REFERENCES

- ABRAMOWITZ, M. & STEGUN, I. A. 1965 *Handbook of Mathematical Functions*. Dover.
- AGARWAL, R. K., YUN, K. Y. & BALAKRISHNAN, R. 2001 Beyond Navier–Stokes: Burnett equations for flows in the continuum–transition regime. *Phys. Fluids* **13** (10), 3061.
- ANDO, N. 2011 The geodesic curvatures of lines of curvature. www.sci.kumamoto-u.ac.jp/~ando/090306.pdf, pp. 1–29.
- ASHURST, WM. T., KERSTEIN, A. R., KERR, R. M. & GIBSON, C. H. 1987 Alignment of vorticity and scalar gradient with strain rate in simulated Navier–Stokes turbulence. *Phys. Fluids* **30** (8), 2343.
- BAKER, L. L. & HADJICONSTANTINO, N. G. 2005 Variance reduction for Monte Carlo solutions of the Boltzmann equation. *Phys. Fluids* **17** (5), 051703.
- BAKER, L. L. & HADJICONSTANTINO, N. G. 2008 Variance-reduced Monte Carlo solutions of the Boltzmann equation for low-speed gas flows: a discontinuous Galerkin formulation. *Intl J. Numer. Meth. Fluids* **58** (4), 381–402.
- BARDOS, C., GOLSE, F. & LEVERMORE, C. D. 1993 Fluid dynamic limits of kinetic equations. Part 2. Convergence proofs for the Boltzmann equation. *Commun. Pure Appl. Math.* **46** (5), 667–753.
- BARDOS, C., GOLSE, F. & LEVERMORE, C. D. 1998 Acoustic equation and Stokes limits for the Boltzmann equation. *C. R. Acad. Sci. I* **327**, 323–328.
- BARGATIN, I., KOZINSKY, I. & ROUKES, M. L. 2007 Efficient electrothermal actuation of multiple modes of high-frequency nanoelectromechanical resonators. *Appl. Phys. Lett.* **90** (9), 093116.
- BATCHELOR, G. K. 1953 *The Theory of Homogeneous Turbulence*. Cambridge University Press.
- BERGER, R., GERBER, C., LANG, H. P. & GIMZEWSKI, J. K. 1997 Micromechanics: a toolbox for femtoscale science: ‘towards a laboratory on a tip’. *Microelectron. Engng* **35** (1–4), 373–379.
- BHATNAGAR, P. L., GROSS, E. P. & KROOK, M. 1954 A model for collision processes in gases. Part 1. Small amplitude processes in charged and neutral one-component systems. *Phys. Rev.* **94** (3), 511.
- BINNIG, G., QUATE, C. F. & GERBER, C. 1986 Atomic force microscope. *Phys. Rev. Lett.* **56** (9), 930–933.
- BIRD, G. A. 1963 Approach to translational equilibrium in a rigid sphere gas. *Phys. Fluids* **6**, 1518–1519.
- BIRD, G. A. 1978 Monte Carlo simulation of gas flows. *Annu. Rev. Fluid Mech.* **10** (1), 11–31.
- BIRD, G. A. 1998 Recent advances and current challenges for DSMC. *Comput. Math. Appl.* **35** (1–2), 1–14.
- BOBYLEV, A. V. 1982 The Chapman–Enskog and Grad methods for solving the Boltzmann equation. *Akad. Nauk SSSR Dokl.* **262**, 71–75.
- BOLTZMANN, L. 1872 Weitere Studien über das Wärmegleichgewicht unter Gasmolekülen. *Wiener Berichte* **66**, 275–370.
- BOSKOVIC, S., CHON, J. W. M., MULVANEY, P. & SADER, J. E. 2002 Rheological measurements using microcantilevers. *J. Rheol.* **46** (4), 891.
- BURG, T. P., GODIN, M., KNUDSEN, S. M., SHEN, W., CARLSON, G., FOSTER, J. S., BABCOCK, K. & MANALIS, S. R. 2007 Weighing of biomolecules, single cells and single nanoparticles in fluid. *Nature* **446** (7139), 1066–1069.
- BURNETT, D. 1935 The distribution of velocities in a slightly non-uniform gas. *Proc. Lond. Math. Soc.* **2** (1), 385.
- CAO, B.-Y., SUN, J., CHEN, M. & GUO, Z.-Y. 2009 Molecular momentum transport at fluid–solid interfaces in MEMS/NEMS: a review. *Intl J. Molecular Sci.* **10** (11), 4638–4706.
- CARTAN, H. 1977 *Course de Calcul Différentiel*. Hermann.
- CERCIGNANI, C. 1962 Elementary solutions of the linearized gas-dynamics Boltzmann equation and their application to the slip-flow problem. *Ann. Phys.* **20** (2), 219–233.
- CERCIGNANI, C. 1964 Higher order slip according to the linearized Boltzmann equation. *Tech. Rep.*, California University Berkeley Institute of Engineering Research.

- CERCIGNANI, C. 1988 *The Boltzmann Equation and its Applications*. Springer.
- CERCIGNANI, C. 2000 *Rarefied Gas Dynamics: From Basic Concepts to Actual Calculations*. Cambridge University Press.
- CHAPMAN, S. 1916 On the law of distribution of molecular velocities, and on the theory of viscosity and thermal conduction, in a non-uniform simple monatomic gas. *Phil. Trans. R. Soc. Lond. Ser. A, Containing Papers of a Mathematical or Physical Character* **216**, 279–348.
- CHAPMAN, S. & COWLING, T. G. 1960 *The Mathematical Theory of Non-uniform Gases*. Cambridge University Press.
- CHEN, H., KANDASAMY, S., ORSZAG, S., SHOCK, R., SUCCI, S. & YAKHOT, V. 2003 Extended Boltzmann kinetic equation for turbulent flows. *Science* **301** (5633), 633–636.
- CHEN, S., CHEN, H., MARTNEZ, D. & MATTHAEUS, W. 1991 Lattice Boltzmann model for simulation of magnetohydrodynamics. *Phys. Rev. Lett.* **67** (27), 3776–3779.
- CHUN, J. & KOCH, D. L. 2005 A direct simulation Monte Carlo method for rarefied gas flows in the limit of small Mach number. *Phys. Fluids* **17** (10), 107107.
- CLELAND, A. N. 2002 *Foundations of Nanomechanics*. Springer.
- CLERCX, H. J. H. & VAN HEIJST, G. J. F. 2009 Two-dimensional Navier–Stokes turbulence in bounded domains. *Appl. Mech. Rev.* **62** (2), 020802.
- COLOSQUI, C. E., KARABACAK, D. M., EKINCI, K. L. & YAKHOT, V. 2010 Lattice Boltzmann simulation of electromechanical resonators in gaseous media. *J. Fluid Mech.* **652**, 241–257.
- CRAIGHEAD, H. G. 2000 Nanoelectromechanical systems. *Science* **290** (5496), 1532–1535.
- ENSKOG, D. 1917 *Kinetische Theorie der Vorgänge in mässig verdünnten Gasen*. PhD thesis, Uppsala.
- FAN, J. & SHEN, C. 2001 Statistical simulation of low-speed rarefied gas flows. *J. Comput. Phys.* **167** (2), 393–412.
- FRISCH, U., HASSLACHER, B. & POMEAU, Y. 1986 Lattice-gas automata for the Navier–Stokes equation. *Phys. Rev. Lett.* **56** (14), 1505–1508.
- GIESSIBL, F. J. 2003 Advances in atomic force microscopy. *Rev. Mod. Phys.* **75** (3), 949–983.
- GRAD, H. 1949 On the kinetic theory of rarefied gases. *Commun. Pure Appl. Math.* **2**, 331–407.
- GRAD, H. 1958 *Principles of the Kinetic Theory of Gases*. Springer.
- GROTH, C. P. T. & McDONALD, J. G. 2009 Towards physically realizable and hyperbolic moment closures for kinetic theory. *Contin. Mech. Thermodyn.* **21** (6), 467–493.
- GU, X.-J. & EMERSON, D. R. 2007 A computational strategy for the regularized 13 moment equations with enhanced wall-boundary conditions. *J. Comput. Phys.* **225** (1), 263–283.
- HADJICONSTANTINO, N. G. 2003 Comment on Cercignani’s second-order slip coefficient. *Phys. Fluids* **15** (8), 2352.
- HADJICONSTANTINO, N. G. 2005a Oscillatory shear-driven gas flows in the transition and free-molecular-flow regimes. *Phys. Fluids* **17** (10), 100611.
- HADJICONSTANTINO, N. G. 2005b Validation of a second-order slip model for dilute gas flows. *Microscale Therm. Engng* **9** (2), 137–153.
- HADJICONSTANTINO, N. G., GARCIA, A. L., BAZANT, M. Z. & HE, G. 2003 Statistical error in particle simulations of hydrodynamic phenomena. *J. Comput. Phys.* **187** (1), 274–297.
- HIGUERA, F. J & JIMÉNEZ, J. 1989 Boltzmann approach to lattice gas simulations. *Europhys. Lett.* **9** (7), 663–668.
- HILBERT, D. 1900 Mathematische Probleme. In *Vortrag, gehalten auf dem internationalen Mathematiker*, pp. 253–297. Vadenhöck and Ruprecht.
- HILBERT, D. 1912 *Grundzüge einer Allgemeinen Theorie der Linearen Integralgleichungen*. Teubner.
- DE IZARRA, L., ROUET, J.-L. & IZRAR, B. 2011 High-order lattice Boltzmann models for gas flow for a wide range of Knudsen numbers. *Phys. Rev. E* **84** (6), 1–7.
- JIN, S. & SLEMRD, M. 2001 Regularization of the Burnett equations via relaxation. *J. Stat. Phys.* **103** (5), 1009–1033.
- KENNARD, E. H. 1938 *Kinetic Theory of Gases*. McGraw-Hill.
- KNUDSEN, M. 1909a Die Gesetze der molekular Strömung und der inneren Reibungsströmung der Gase durch Röhren. *Ann. Phys.* **28**, 75–130.

- KNUDSEN, M. 1909*b* Eine Revision der Gleichgewichtsbedingung der Gase: Thermische Molekularströmung. *Ann. Phys.* **336** (1), 205–229.
- LAGUBEAU, G., LE MERRER, M., CLANET, C. & QUÉRÉ, D. 2011 Leidenfrost on a ratchet. *Nat. Phys.* **7** (5), 395–398.
- LAVRIK, N. V., SEPANIAK, M. J. & DATSKOS, P. G. 2004 Cantilever transducers as a platform for chemical and biological sensors. *Rev. Sci. Instrum.* **75** (7), 2229.
- LEE, C. J. 1994 Unique determination of solutions to the Burnett equations. *AIAA J.* **32**, 985–990.
- LOYALKA, S. K. 1971 Kinetic theory of thermal transpiration and mechanocaloric effect. Part 1. *J. Chem. Phys.* **55** (9), 4497.
- LOYALKA, S. K., PETRELLIS, N. & STORVICK, T. S. 1979 Some exact numerical results for the BGK model: Couette, Poiseuille and thermal creep flow between parallel plates. *Z. Angew. Math. Phys.* **30** (3), 514–521.
- MANELA, A. & HADJICONSTANTINOY, N. G. 2010 Gas-flow animation by unsteady heating in a microchannel. *Phys. Fluids* **22** (6), 062001.
- MAURER, J., TABELING, P., JOSEPH, P. & WILLAIME, H. 2003 Second-order slip laws in microchannels for helium and nitrogen. *Phys. Fluids* **15** (9), 2613.
- MAXWELL, J. C. 1878 On stresses in rarefied gases arising from inequalities of temperature. *Proc. R. Soc. Lond.* **27** (185–189), 304–308.
- MAXWELL, J. C. 1879 On stresses in rarified gases arising from inequalities of temperature. *Phil. Trans. R. Soc. Lond.* **170**, 231–256.
- MCMANARA, G. & ZANETTI, G. 1988 Use of the Boltzmann equation to simulate lattice gas automata. *Phys. Rev. Lett.* **61** (20), 2332–2335.
- MOTAMEDI, R. & WOOD-ADAMS, P. M. 2010 Measurement of fluid properties using an acoustically excited atomic force microscope micro-cantilever. *J. Rheol.* **54** (5), 959.
- OHWADA, T. & SONE, Y. 1992 Analysis of thermal stress slip flow and negative thermophoresis using the Boltzmann equation for hard-sphere molecules. *Eur. J. Mech. B* **11** (4), 389–414.
- OHWADA, T., SONE, Y. & AOKI, K. 1989*a* Numerical analysis of the Poiseuille and thermal transpiration flows between two parallel plates on the basis of the Boltzmann equation for hard-sphere molecules. *Phys. Fluids A* **1** (12), 2042.
- OHWADA, T., SONE, Y. & AOKI, K. 1989*b* Numerical analysis of the shear and thermal creep flows of a rarefied gas over a plane wall on the basis of the linearized Boltzmann equation for hard-sphere molecules. *Phys. Fluids A* **1** (9), 1588–1599.
- ONISHI, Y. & SONE, Y. 1979 Kinetic theory of slightly strong evaporation and condensation: hydrodynamic equation and slip boundary condition for finite Reynolds number. *J. Phys. Soc. Japan* **47** (5), 1676–1685.
- ORSZAG, S. A. & KELLS, L. C. 1980 Transition to turbulence in plane Poiseuille and plane Couette flow. *J. Fluid Mech.* **96**, 159–205.
- PARK, J. H., BAHUKUDUMBI, P. & BESKOK, A. 2004 Rarefaction effects on shear driven oscillatory gas flows: a direct simulation Monte Carlo study in the entire Knudsen regime. *Phys. Fluids* **16** (2), 317.
- PITAKARNNOP, J., VAROUTIS, S., VALOUGEORGIS, D., GEOFFROY, S., BALDAS, L. & COLIN, S. 2009 A novel experimental setup for gas microflows. *Microfluid. Nanofluid.* **8** (1), 57–72.
- POZRIKIDIS, C. 1992 *Boundary Integral and Singularity Methods for Linearized Viscous Flow*. Cambridge University Press.
- PRANDTL, L. 1904 Über Flüssigkeitsbewegung bei sehr kleiner Reibung. In *Proceedings of 3rd International Mathematics Congress, Heidelberg* (ed. A. Krazer), pp. 484–491. Teubner.
- QIAN, Y.-H., D'HUMIÈRES, D. & LALLEMAND, P. 1992 Lattice BGK models for Navier–Stokes equation. *Europhys. Lett.* **17** (6), 479.
- RADTKE, G. A., HADJICONSTANTINOY, N. G. & WAGNER, W. 2011 Low-noise Monte Carlo simulation of the variable hard sphere gas. *Phys. Fluids* **23** (3), 030606.
- RAMANATHAN, S. & KOCH, D. L. 2009 An efficient direct simulation Monte Carlo method for low Mach number noncontinuum gas flows based on the Bhatnagar–Gross–Krook model. *Phys. Fluids* **21** (3), 033103.
- RAMANATHAN, S., KOCH, D. L. & BHILADVALA, R. B. 2010 Noncontinuum drag force on a nanowire vibrating normal to a wall: simulations and theory. *Phys. Fluids* **22** (10), 103101.

- REYNOLDS, O. 1879 On certain dimensional properties of matter in the gaseous state. Part 1. Experimental researches on thermal transpiration of gases through porous plates and on the laws of transpiration and impulsion, including an experimental proof that gas is not a continuous plenum. *Phil. Trans. R. Soc. Lond.* **170**, 727–845.
- REYNOLDS, O. 1883 An experimental investigation of the circumstances which determine whether the motion of water shall be direct or sinuous, and of the law of resistance in parallel channels. *Proc. R. Soc. Lond.* **35** (224–226), 84.
- REYNOLDS, O. 1895 On the dynamical theory of incompressible viscous fluids and the determination of the criterion. *Phil. Trans. R. Soc. Lond. A* **186**, 123–164.
- SADER, J. E. 1998 Frequency response of cantilever beams immersed in viscous fluids with applications to the atomic force microscope. *J. Appl. Phys.* **84** (1), 64.
- SCHLICHTING, H. 1960 *Boundary-Layer Theory*. McGraw-Hill.
- SHARIPOV, F. & KALEMPA, D. 2007 Gas flow near a plate oscillating longitudinally with an arbitrary frequency. *Phys. Fluids* **19** (1), 017110.
- SHARIPOV, F. & KALEMPA, D. 2008 Oscillatory Couette flow at arbitrary oscillation frequency over the whole range of the Knudsen number. *Microfluid. Nanofluid.* **4** (5), 363–374.
- SHAVALIYEV, M. S. 1993 Super-Burnett corrections to the stress tensor and the heat flux in a gas of Maxwellian molecules. *J. Appl. Math. Mech.* **57** (3), 573–576.
- SHEN, S., CHEN, G., CRONE, R. M. & ANAYA-DUFRESNE, M. 2007 A kinetic-theory based first order slip boundary condition for gas flow. *Phys. Fluids* **19** (8), 086101.
- SHI, Y., BROOKES, P., YAP, Y. & SADER, J. E. 2011 Accuracy of the lattice Boltzmann method for low-speed noncontinuum flows. *Phys. Rev. E* **83** (4), 2–5.
- SHI, Y. & SADER, J. E. 2010 Lattice Boltzmann method for oscillatory Stokes flow with applications to micro- and nanodevices. *Phys. Rev. E* **81** (3), 1–14.
- SODERHOLM, L. H. 2007 Hybrid Burnett equations: a new method of stabilizing. *Transp. Theory Stat. Phys.* **36** (4), 495–512.
- SONE, Y. 1964 Kinetic theory analysis of linearized Rayleigh problem. *J. Phys. Soc. Japan* **19** (8), 1463–1473.
- SONE, Y. 1965 Effect of sudden change of wall temperature in rarefied gas. *J. Phys. Soc. Japan* **20** (2), 222–229.
- SONE, Y. 1966 Thermal creep in rarefied gas. *J. Phys. Soc. Japan* **21**, 1836–1837.
- SONE, Y. 1968a Asymptotic behaviour of diffusion of tangential velocity discontinuity in rarefied gas. *Phys. Fluids* **11**, 1935.
- SONE, Y. 1968b Flow of rarefied gas through a circular pipe. *Phys. Fluids* **11**, 1672.
- SONE, Y. 1969 Asymptotic theory of flow of rarefied gas over a smooth boundary. Part 1. In *Rarefied Gas Dynamics* (ed. L. Trilling & H. Y. Wachman), pp. 243–253. Academic.
- SONE, Y. 1974 Asymptotic theory of flow of rarefied gas over a smooth boundary. Part 2. *Trans. Japan Soc. Aeronaut. Space Sci.* **17**, 113–122.
- SONE, Y. 2000 *Kinetic Theory and Fluid Dynamics*. Birkhäuser.
- SONE, Y. 2007 *Molecular Gas Dynamics: Theory, Techniques, and Applications*. Springer.
- SONE, Y., OHWADA, T. & AOKI, K. 1989 Temperature jump and Knudsen layer in a rarefied gas over a plane wall: numerical analysis of the linearized Boltzmann equation for hard-sphere molecules. *Phys. Fluids. A, Fluid Dyn.* **1** (2), 363–370.
- SONE, Y. & ONISHI, Y. 1973 Kinetic theory of evaporation and condensation. *J. Phys. Soc. Japan* **35** (6), 1773–1776.
- SONE, Y. & ONISHI, Y. 1978 Kinetic theory of evaporation and condensation: hydrodynamic equation and slip boundary condition. *J. Phys. Soc. Japan* **44** (6), 1981–1994.
- STOKES, G. G. 1851 On the effect of the internal friction of fluids on the motion of pendulums. *Trans. Camb. Phil. Soc.* **9**, 8–106.
- STRUCHTRUP, H. 2005 Failures of the Burnett and super-Burnett equations in steady state processes. *Contin. Mech. Thermodyn.* **17** (1), 43–50.
- STRUCHTRUP, H. & TORRILHON, M. 2003 Regularization of Grad's 13 moment equations: derivation and linear analysis. *Phys. Fluids* **15** (9), 2668.

- TAKATA, S., AOKI, K., HATTORI, M. & HADJICONSTANTINO, N. G. 2012 Parabolic temperature profile and second-order temperature jump of a slightly rarefied gas in an unsteady two-surface problem. *Phys. Fluids* **24** (3), 032002.
- TANG, G., GU, X.-J., BARBER, R., EMERSON, D. R. & ZHANG, Y. 2008 Lattice Boltzmann simulation of nonequilibrium effects in oscillatory gas flow. *Phys. Rev. E* **78** (2), 1–8.
- TIBBS, K. W., BARAS, F. & GARCIA, A. L. 1997 Anomalous flow profile due to the curvature effect on slip length. *Phys. Rev. E* **56** (2), 2282–2283.
- TORRILHON, M. & STRUCHTRUP, H. 2008 Boundary conditions for regularized 13-moment-equations for micro-channel-flows. *J. Comput. Phys.* **227** (3), 1982–2011.
- VARGO, S. E., MUNTZ, E. P., SHIFLETT, G. R. & TANG, W. C. 1999 Knudsen compressor as a micro- and macroscale vacuum pump without moving parts or fluids. *J. Vac. Sci. Technol. A* **17** (4), 2308.
- VINCENTI, W. G. & KRUGER, C. H. JR. 1965 *Introduction to Physical Gas Dynamics*, 8th edition. Krieger.
- WELANDER, P. 1954 On the temperature jump in a rarefied gas. *Arkiv Fysik* **7**, 507–553.
- WENG, H. C. & CHEN, C.-K. 2008 A challenge in Navier–Stokes-based continuum modelling: Maxwell–Burnett slip law. *Phys. Fluids* **20** (10), 106101.
- WILLIAMS, M. M. R. 1971 Boundary-value problems in the kinetic theory of gases. Part 2. Thermal creep. *J. Fluid Mech.* **45** (04), 759.
- WÜRGER, A. 2011 Leidenfrost gas ratchets driven by thermal creep. *Phys. Rev. Lett.* **107** (16), 1–4.
- YANG, Y. T., CALLEGARI, C., FENG, X. L., EKINCI, K. L. & ROUKES, M. L. 2006 Zeptogram-scale nanomechanical mass sensing. *Nano Lett.* **6** (4), 583–586.
- YAP, Y. W. & SADER, J. E. 2012 High accuracy numerical solutions of the Boltzmann Bhatnagar–Gross–Krook equation for steady and oscillatory Couette flows. *Phys. Fluids* **24** (3), 032004.
- YU, H., GIRIMAJI, S. & LUO, L.-S. 2005 Lattice Boltzmann simulations of decaying homogeneous isotropic turbulence. *Phys. Rev. E* **71** (1), 1–5.
- ZHONG, X., MACCORMACK, R. W. & CHAPMAN, D. R. 1993 Stabilization of the Burnett equations and application to hypersonic flows. *AIAA J.* **31** (6), 1036–1043.